



## Ultraviolet and visible radiation at Barrow, Alaska: Climatology and influencing factors on the basis of version 2 National Science Foundation network data

Germar Bernhard,<sup>1</sup> Charles R. Booth,<sup>1</sup> James C. Ehramjian,<sup>1</sup> Robert Stone,<sup>2,3</sup> and Ellsworth G. Dutton<sup>2</sup>

Received 1 August 2006; revised 28 November 2006; accepted 15 December 2006; published 2 May 2007.

[1] Spectral ultraviolet (UV) and visible irradiance has been measured near Barrow, Alaska (71°N, 157°W), between 1991 and 2005 with a SUV-100 spectroradiometer. The instrument is part of the U.S. National Science Foundation's UV Monitoring Network. Here we present results based on the recently produced "version 2" data release, which supersedes published "version 0" data. Cosine error and wavelength-shift corrections applied to the new version increased biologically effective UV dose rates by 0–10%. Corrected clear-sky measurements of different years are typically consistent to within  $\pm 3\%$ . Measurements were complemented with radiative transfer model calculations to retrieve total ozone and surface albedo from measured spectra and for the separation of the different factors influencing UV and visible radiation. A climatology of UV and visible radiation was established, focusing on annual cycles, trends, and the effect of clouds. During several episodes in spring of abnormally low total ozone, the daily UV dose at 305 nm exceeded the climatological mean by up to a factor of 2.6. Typical noontime UV Indices during summer vary between 2 and 4; the highest UV Index measured was 5.0 and occurred when surface albedo was unusually high. Radiation levels in the UV-A and visible exhibit a strong spring-autumn asymmetry. Irradiance at 345 nm peaks on approximately 20 May, 1 month before the solstice. This asymmetry is caused by increased cloudiness in autumn and high albedo in spring, when the snow covered surface enhances downwelling UV irradiance by up to 57%. Clouds reduce UV radiation at 345 nm on average by 4% in March and by more than 40% in August. Aerosols reduce UV by typically 5%, but larger reductions were observed during Arctic haze events. Stratospheric aerosols from the Pinatubo eruption in 1991 enhanced spectral irradiance at 305 nm for large solar zenith angles. The year-to-year variations of spectral irradiance at 305 nm and of the UV Index are mostly caused by variations in total ozone and cloudiness. Changes in surface albedo that may occur in the future can have a marked impact on UV levels between May and July. No statistically significant trends in monthly mean noontime irradiance were found.

**Citation:** Bernhard, G., C. R. Booth, J. C. Ehramjian, R. Stone, and E. G. Dutton (2007), Ultraviolet and visible radiation at Barrow, Alaska: Climatology and influencing factors on the basis of version 2 National Science Foundation network data, *J. Geophys. Res.*, *112*, D09101, doi:10.1029/2006JD007865.

### 1. Introduction

[2] Solar UV radiation reaching the Earth's surface has a wide range of effects on humans as well as aquatic and terrestrial ecosystems [*United Nations Environmental Program*, 2003]. Exposure to UV radiation has been linked to sunburn, skin cancer, corneal damage, and cataracts in

humans. Beneficial effects of UV radiation include the photochemical production of Vitamin D in the skin [*Lehmann*, 2005]. Vitamin D is essential for the formation of bones [*Holick*, 1996] and may also protect from internal cancers such as prostate, breast, and colon cancer [*Moon et al.*, 2005]. The ambivalence of detrimental and beneficial UV effects is of particular interest in the Arctic: on one hand, reflections off snow covered surfaces and long hours of sunshine during summer months can lead to considerable UV exposure [*Cockell et al.*, 2001]. On the other hand, the virtual absence of UV-B radiation during winter months may result in Vitamin D deficiency [*Webb et al.*, 1988; *Engelsen et al.*, 2005] and associated diseases such as rickets [*Stokstad*, 2003].

[3] Stratospheric ozone depletion and climate change (e.g., changes in surface albedo and cloudiness) may further

<sup>1</sup>Biospherical Instruments Inc., San Diego, California, USA.

<sup>2</sup>Global Monitoring Division, Earth System Research Laboratory, NOAA, Boulder, Colorado, USA.

<sup>3</sup>Also at Cooperative Institute for Research in Environmental Science, University of Colorado, Boulder, Colorado, USA.

modify the UV climate in the Arctic and consequences for the biosphere are anticipated [*Arctic Climate Impact Assessment (ACIA)*, 2005]. Ozone decreases in the Arctic are fortunately less severe than in the Antarctic because of higher stratospheric temperatures in the North, which make the formation of polar stratospheric clouds and the photochemical destruction of ozone less prevalent [*World Meteorological Organization (WMO)*, 2003]. However, in years when the polar vortex was strong and stratospheric temperatures remained cold (e.g., 1993, 1997), photochemically induced decreases in total ozone of up to 45% have been observed over vast areas of Europe and Siberia [*ACIA*, 2005; *Newman et al.*, 1997]. Reductions of ozone over Alaska have been somewhat smaller because of a combination of decadal variations in the circulation and transport of ozone depleted air from the polar vortex [*Knudsen and Andersen*, 2001]. The trend in mean annual total column ozone over the Arctic was approximately  $-3\%$  per decade for the period from 1979 to 2000 (a total decrease of about 7%). The trend in mean spring total column ozone was approximately  $-5\%$  per decade for the period from 1979 to 2000 (a total decrease of 11%) [*ACIA*, 2005]. The biggest ozone losses ever recorded over the Arctic were observed in 2005, when about one third of ozone molecules were destroyed in the arctic stratosphere [*Schiermeier*, 2005].

[4] UV measurements in the Arctic are sparse and are mainly performed in Alaska, Canada, Greenland, and Scandinavia [*ACIA*, 2005]. We are not aware of any measurements in the Russian Arctic. Here we present UV measurements at Barrow, Alaska, performed with a high-resolution SUV-100 spectroradiometer from Biospherical Instruments Inc (BSI). The instrument is part of the U.S. National Science Foundation's Office of Polar Programs (NSF/OPP) Ultraviolet Spectral Irradiance Monitoring Network [*Booth et al.*, 1994]. The network currently consists of seven mostly high-latitude sites and is operated by BSI. All stations measure global spectral irradiance between 280 and 600 nm. Further information on the network is available at the Web site <http://www.biospherical.com/nsf>.

[5] Most studies that have used network data were based on the originally released "version 0" data set. This data set has not been corrected for deviations of the angular response of SUV-100 spectroradiometers from the ideal cosine response (i.e., the cosine-error [*Seckmeyer et al.*, 2001]) nor for wavelength errors of approximately 0.1 nm, which affect spectra measured before 1997. To improve the accuracy of network data, a new data edition named "version 2" is currently in preparation. Version 2 data are not "pure" measurements like version 0 data because radiative transfer calculations were used for cosine and wavelength error corrections. Version 2 data of network instruments located at the Antarctic sites South Pole ( $90^{\circ}\text{S}$ ), Palmer Station ( $64^{\circ}46'\text{S}$ ,  $64^{\circ}03'\text{W}$ ), and McMurdo Station ( $77^{\circ}50'\text{S}$ ,  $166^{\circ}40'\text{E}$ ) are already available [*Bernhard et al.*, 2004, 2005b, 2006]. This paper introduces the new version 2 data set for the instrument installed at Barrow, Alaska.

## 2. Data Analysis

### 2.1. Instrumentation and Location

[6] Measurements of global (Sun and sky) spectral irradiance were performed approximately 5.5 km northeast of

Barrow, Alaska, between January 1991 and May 2005 with a high-resolution SUV-100 spectroradiometer from BSI. The instrument measures solar spectra between 280 and 600 nm with a resolution of approximately 1.0 nm at a rate of 4 spectra per hour (1 spectrum per hour before April 1997) [*Booth et al.*, 1994; *Bernhard et al.*, 2005a]. It is radiometrically calibrated every 2 weeks using 200-Watt tungsten-halogen lamps, which are traceable to the source-based spectral irradiance scale that was realized in 1990 by the National Institute of Standards and Technology (NIST) [*Yoon et al.*, 2002]. More details on calibration and quality control of version 0 data can be found in Network Operations Reports [e.g., *Bernhard et al.*, 2005a]. The instrument is installed into the roof of the Ukpeaġvik Iñupiat Corporation building ( $71^{\circ}19'29''\text{N}$ ,  $156^{\circ}40'45''\text{W}$ , 8 m above sea level). Point Barrow, the northernmost point of Alaska, is located 10 km northeast of the instrument. The Chukchi Sea is 300 m northwest of the system and typically covered by ice between November and July. The coastline runs from southwest to northeast. The land south and east of the system is flat tundra covered with grasses, sedges, and mosses. During the summer months much of the area is covered by shallow ponds (thaw lakes). Snow cover roughly extends from October to June [*Stone et al.*, 2002]. Annual cycles in sea ice and snow cover cause a large difference of surface albedo between summer and winter. Particularly in the spring, the area is affected by "Arctic haze," a circumpolar phenomenon, which partly originates from anthropogenic pollution emissions in Europe and the former Soviet Union [*Bodhaine and Dutton*, 1993]. Arctic haze can lead to aerosol optical depths in excess of 0.3. Dust and smoke from boreal forest fires are also important contributors to the aerosols burden [*Damoah et al.*, 2004]. Clouds are frequent in any month but have a larger optical depth in autumn than in spring. *Dutton et al.* [2004] found a statistically significant upward trend in cloud occurrence frequency of 76 to 82% between 1976 and 2001. General weather conditions and the radiation climate have been characterized by *Maykut and Church* [1973].

### 2.2. Radiative Transfer Calculations

[7] Measurements were complemented with model calculations performed with the radiative transfer model UVSPEC/libradtran version 1.01, available at [www.libradtran.org](http://www.libradtran.org) [*Mayer and Kylling*, 2005]. The model's double-precision pseudospherical disort radiative transfer solver with six streams and 50 layers was used.

[8] The extraterrestrial spectrum (ETS) used for modeling is based on the ETS recently proposed by *Gueymard* [2004]. Since the resolution of this spectrum is not sufficient to be used directly in the model, we superimposed the fine structure from the "Kitt Peak solar flux atlas" [*Kurucz et al.*, 1984]. The composite spectrum is identical with the spectrum  $E_{\text{Gueymard}}(\lambda)$  described by *Bernhard et al.* [2004, hereinafter referred to as *B04*]. Air density, pressure, and  $\text{NO}_2$  profiles were taken from *Anderson et al.* [1986]. The total  $\text{NO}_2$  column was set to 0.19 DU, which is a typical value for summer months in the Arctic [*Richter et al.*, 2005]. Rayleigh scattering optical depth by *Bodhaine et al.* [1999] was implemented. Surface pressure was measured at the Barrow Observatory of NOAA's Earth System Research Laboratory (ESRL) (formerly Climate Monitoring

**Table 1.** Instruments to Measure Aerosol Optical Depth

Instrument	Period	Wavelengths, nm	Wavelengths Used for Calculation of $\alpha$ , nm	Wavelengths Used for Calculation of $\beta$ , nm	Affiliation
Carter-Scott SP 1-A	16 Mar 2000 to 29 Apr 2002	367, 413, 499, 862	413, 499	499	ESRL
Carter-Scott SP 02	9 Mar 2001 to 12 Jun 2001	412, 500, 675, 862	500, 675	500	ESRL
Carter-Scott SP 02	19 Feb 2002 to 23 Apr 2002	412, 500, 675, 862	412, 500	500	ESRL
Carter-Scott SP 02 <sup>a</sup>	19 Feb 2002 to 11 Oct 2002	411, 500, 675, 862			ESRL
Carter-Scott SP 01 <sup>a</sup>	16 Feb 2003 to 31 Oct 2005	413, 499, 675, 865			ESRL
Cimel CE 318N	26 Jun 1999 to 27 Sep 1999; 27 Mar 2002 to 1 Oct 2002; 5 May 2004 to 2 Oct 2004	340, 380, 440, 500, 675, 870, 1020	340, 500	500	NASA/AERONET
FWNIP <sup>b</sup>	23 Jan 1991 to 13 May 2005	approximately 500 nm, wideband	parameterized	500	ESRL

<sup>a</sup>Only used for validation of FWNIP measurements (Figure 1); not used for model calculations of version 2 UV data.

<sup>b</sup>Several FWNIP measurements per day are typically performed when the Sun is visible. Observations in some years were performed less frequently.

and Diagnostics Laboratory, CMDL) 2 km east of the spectroradiometer. Total column ozone was calculated from measured UV spectra using a method described and validated by *Bernhard et al.* [2003]. For these calculation, the *Bass and Paur* [1985] ozone absorption cross section and ozone profiles measured by the Solar Backscatter Ultraviolet Radiometer 2 (SBUV/2) on board the NOAA 11 satellite were used. Profiles from several years were averaged over 14-day periods to provide climatological mean profiles. More details on the handling of ozone profiles and the temperature dependence of the ozone absorption cross section are given by *Bernhard et al.* [2003]. Effective surface albedo was calculated from UV spectra as described in section 3.2. The method is only applicable for periods of clear skies. Clear-sky spectra were selected from the data set based on temporal variability of spectral irradiance at 600 nm using a similar method to that described by *B04*. Effective surface albedo for cloudy days was linearly interpolated from the clear-sky data set. Uncertainties related to the interpolation scheme are discussed in section 3.2. Modeled spectra were convolved with a triangular function of 1.0 nm full width at half maximum (FWHM).

### 2.3. Aerosol Parameterization

[9] Aerosols have a large effect on the ratio of direct and diffuse irradiance, which is an important parameter for the cosine error correction. Furthermore, aerosols can attenuate global irradiance by several percent and are an essential parameter for interpreting clear-sky UV irradiance. Great attention was therefore given to the parameterization of aerosols in the radiative transfer model.

#### 2.3.1. Aerosol Optical Depth and Ångström Coefficients

[10] Aerosol extinction  $\tau(\lambda)$  was parameterized in the model with Ångström's turbidity formula:

$$\tau(\lambda) = \beta \lambda^{-\alpha}. \quad (1)$$

The Ångström coefficients  $\alpha$  and  $\beta$  were calculated from aerosol optical depth (AOD) measurements of various instruments including Carter-Scott and Cimel Sun photometers (Table 1). The latter instrument is part of NASA's Aerosol Robotic Network (AERONET) and located next to the ESRL station at the research facility of the Atmospheric Radiation Measurement (ARM) program. During years when no Sun photometer data were available, measurements

of a Filter Wheel Normal Incidence Pyrheliometer (FWNIP) operated by ESRL were used. The instrument provides stable estimate of mean visible aerosol optical depth but has a lower accuracy than data from Sun photometers [*Dutton and Christy*, 1992]. Figure 1e shows a comparison of FWNIP measurements with measurements of  $\tau(500 \text{ nm})$  performed by Carter-Scott and Cimel Sun photometers, demonstrating that FWNIP data are a reasonably good proxy of  $\tau(500 \text{ nm})$ . The standard deviation of the difference of FWNIP measurements and Sun photometer AODs is 0.03.

[11] For data of the Carter-Scott and Cimel instruments, the Ångström coefficient  $\alpha$  were calculated from AOD measurements at two different wavelengths, which are indicated in Table 1. For FWNIP data,  $\alpha$  was parameterized with the expression:

$$\alpha = 0.05 + 2e^{-4\tau(500\text{nm})}, \quad (2)$$

where  $\tau(500 \text{ nm})$  was set equal to the reading of the FWNIP instrument. The parameterization was established by fitting an exponential function of the form  $a + b \exp[-c\tau(500 \text{ nm})]$  to a scatterplot of  $\alpha$  versus  $\tau(500 \text{ nm})$  using data of the Cimel instrument. A similar relationship between  $\alpha$  and  $\tau(500 \text{ nm})$  has recently been derived from aerosol measurements at various Arctic and Antarctic locations [*Climate Monitoring Diagnostics Laboratory (CMDL)*, 2004, Figure 3.32]. The physics behind this parameterization is that aerosols of different type and origin (e.g., continental or marine) tend to have different size distributions (which are related to  $\alpha$ ) and different AODs. For example, background aerosols in the Arctic are predominantly small (leading to large values of  $\alpha$ ) and have small AOD. In contrast, haze and dust events are governed by larger particles with small  $\alpha$  and large AOD. The parameterization may not be adequate for all conditions, such as smoke events, but is a viable approach in absence of other data. We also note that the parameterization was derived from measurements at Barrow and cannot be applied to other locations. To validate the approach, AODs at various wavelengths were estimated from FWNIP measurements with equations (1) and (2) and compared with AODs measured by the two Sun photometers. Results shown in Figure 1 demonstrate the validity of the method.

#### 2.3.2. Aerosol Profile and Pinatubo Aerosol

[12] For years 1991 and 1995–2005, the vertical distribution of aerosol extinction was parameterized in the model with the aerosol profile for background spring/summer

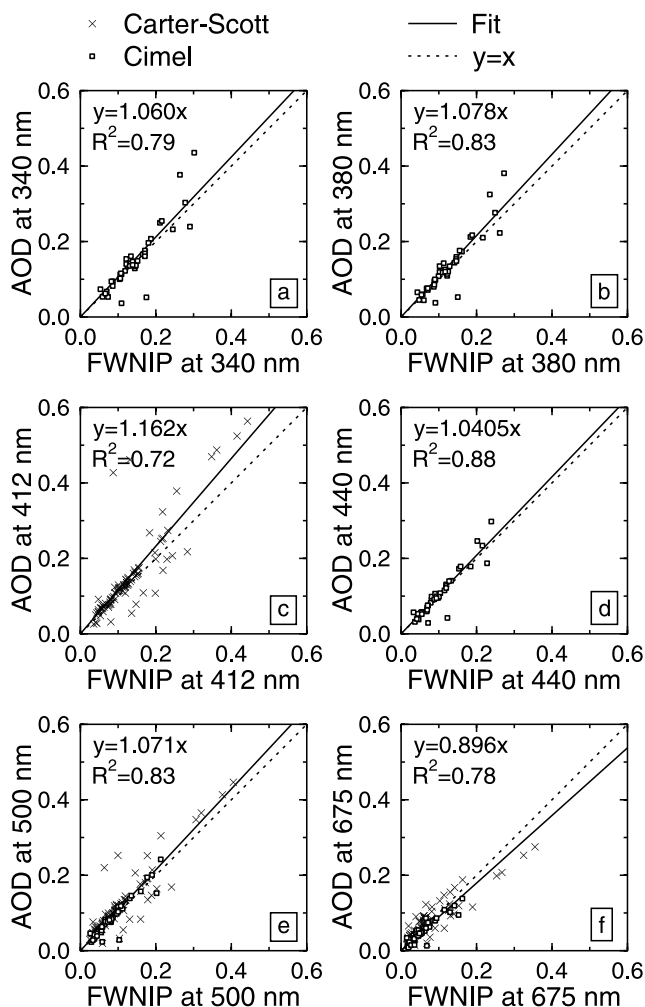


**Figure 1.** Correlations of AOD reconstructed from FWNIP measurements (abscissa) with AOD measurements of Carter-Scott and Cimel Sun photometers (ordinate) at (a) 340 nm, (b) 380 nm, (c) 412 nm, (d) 440 nm, (e) 500 nm, and (f) 675 nm. Solid lines represent least squares fits of functions of the form  $y = sx$  to the data. Scale factors  $s$  and regression coefficients  $R^2$  are given in the top left corner of each panel. For all data points, FWNIP and photometer data were measured less than 15 min apart. FWNIP AODs at 500 nm (Figure 1e) are identical with FWNIP measurements. For other wavelengths, FWNIP AODs were reconstructed using the parameterization described in the text.

conditions suggested by Shettle [1989]. The profile was scaled to match the AOD calculated with equation (1). For periods when the aerosol optical depth was larger than the background AOD (e.g., when Arctic haze was present [Bodhaine and Dutton, 1993]), the vertical distribution was further modified by UVSPEC by placing the excess aerosol into the lowest 2 km of the profile. Following the eruption of Mt. Pinatubo in June 1991 [Self et al., 1996], large amounts of debris and sulfur dioxide gas were injected into the stratosphere, dispersed by upper level winds, and converted to aerosol with an e-folding time of about 24 days [Rosen et al., 1994]. Pinatubo aerosol entered the Arctic stratosphere as early as August before the north polar

vortex had formed [Neuber et al., 1994]. The stratospheric aerosol optical depth at Barrow was 0.19 by April 1992, and gradually decayed with an e-folding time constant of 13.3 months [Stone et al., 1993]. To account for stratospheric aerosols in the model, the aerosol profiles described as “extreme,” “high,” and “moderate” by Shettle [1989] were used for the years 1992, 1993, and 1994, respectively. Photons scattered downward by aerosols that are located within or above the ozone layer can have a shorter path through the ozone layer than unscattered photons [Davies, 1993]. This can lead to a large enhancement of ground-level UV-B irradiance at small wavelengths and large SZAs. The magnitude of the enhancement is very sensitive to the height and distribution of the aerosol layer [Davies, 1993]. Uncertainties in model calculations caused by insufficient knowledge of the aerosol’s vertical distribution are discussed in section 5.

[13] The AOD derived from FWNIP measurements during April 1992 was about 0.3. The associated value for  $\alpha$  calculated with equation (2) is 0.65, which is a comparatively small value. Measurements of the stratospheric aerosol optical depth by aircraft in April 1992 showed very little dependence on wavelength [Stone et al., 1993], also indicating small values of  $\alpha$ . Equation (2) was therefore applied for the period affected by Pinatubo aerosols also, despite the fact that it is based on a parameterization of tropospheric aerosol extinction.

### 2.3.3. Aerosol Single Scattering Albedo and Asymmetry Factor

[14] Aerosol single scattering albedo (SSA) used in the model was calculated from ground-based nephelometer measurements performed by ESRL at Barrow [CMDL, 2004]. The average SSA of the years 1991–2005 is  $0.95 \pm 0.02$  ( $\pm 1\sigma$ ). The SSA of stratospheric sulfuric acid aerosols is typically 0.99 [Vogelmann et al., 1992]. In the absence of actual measurements of stratospheric SSA, we used the values of ground-based SSA measurements for all altitudes. The model asymmetry factor  $g$  was set to 0.65. This value was estimated from measurement of the hemispheric backscatter fraction performed at the ESRL station [CMDL, 2004] using the conversion method by Marshall et al. [1995].

### 2.4. Corrections Applied to Version 2 Data

[15] Version 2 data for Barrow were derived from version 0 data using the same procedures as applied to data from South Pole Station [B04], Palmer Station [Bernhard et al., 2005b], and McMurdo Station [Bernhard et al., 2006]. These algorithms were described in great detail by B04 and only a short summary is given here.

[16] Wavelength shifts have been corrected by correlating the Fraunhofer line structure in measured spectra to the corresponding structure in modeled spectra. Residual wavelength uncertainties after correction are on average  $\pm 0.03$  nm ( $\pm 1\sigma$ ).

[17] Correcting the cosine error [Seckmeyer et al., 2001] of the SUV-100 spectroradiometer at Barrow was challenging because characterizations of the error prior to deployment of the SUV-100 were not applicable to the assembled and installed instrument. Up to 15 November 1993, the instrument’s cosine diffuser (made from polytetrafluoroethylene (PTFE)) was semitransparent at wavelengths longer than 500 nm. This led to a substantial, wavelength-dependent

cosine error, which could not be corrected. Measurements of volumes 2–4 (1991–1993) at wavelengths above 490 nm were not used for further analysis. Data at shorter wavelengths were not affected. The diffuser assembly was replaced in November 1993 with one that did not have this problem. The system's sensitivity with the new collector was somewhat dependent on the azimuth position of the Sun. Magnitude and phase of the azimuthal asymmetry also changed during instrument service. The collector was again modified in December 2000. Azimuthal asymmetries of measurements following the modification were smaller than  $\pm 2\%$  ( $\pm 1\sigma$ ), but the average cosine error increased slightly.

[18] Angular response errors for all data volumes were estimated from comparisons of measurement and model under clear-sky conditions using the Sun as light source as described by *B04*. The accuracy of this method depends critically on the knowledge of the ratio of direct to global irradiance, which in turn is greatly affected by the atmospheric aerosol content. The ratio was estimated with the model. Availability of AOD data from AERONET and ESRL helped in reducing the uncertainty of these calculations. The parameterization of cosine errors derived with this approach was further confirmed with measurements of a test apparatus and solar data from the volume 14 period (2004–2005).

[19] The cosine-error was corrected by multiplying version 0 data with correction factors, which were determined separately for every data volume. Factors are generally smaller than 5% for overcast conditions and become dependent on wavelength, SZA, and other parameters for clear skies. For wavelengths below 340 nm, correction factors vary between 0.97 and 1.07 and depend only little on SZA. At 400 nm, correction factors are between 0.99 and 1.06 at SZA = 50°, and between 0.95 and 1.10 at SZA = 75°. Correction factors are highest at 600 nm: ranges are 0.99 to 1.06 at 50°, 0.95 to 1.18 at 70°, and 0.84 to 1.28 at 82° (overall maximum).

[20] Cosine-error corrected and uncorrected SUV-100 data were also compared with measurements of a collocated GUV-511 multichannel filter radiometer. Differences between SUV-100 and GUV-511 data could be quantitatively explained with the different angular response of the two instruments. More information on the cosine error parameterization, the measurements with the test apparatus, the comparison with the GUV-511 radiometer, the range of correction factors, and the validation of the cosine-error correction method is available at the Web site <http://www.biospherical.com/nsf/Version2/>, hereinafter referred to as “version 2 Web site.”

[21] The bandwidth of SUV-100 spectroradiometers varies between 0.9 and 1.1 nm in the UV-B and between 0.7 and 0.9 nm in the visible. Processing of version 2 data involved normalization of all spectra to a uniform bandwidth of 1.0 nm and resampling of spectra to uniform wavelength step intervals [*B04*].

## 2.5. Uncertainty Budget

[22] A detailed analysis of the uncertainty of version 2 data for Barrow is available at the version 2 Web site and only a summary is given here. Expanded relative uncertainties (coverage factor  $k = 2$ , equal to uncertainties at the  $2\sigma$ -level or a confidence interval of 95.45%) vary between 4.8% and 11.4%.

[23] For volumes 2–4 (1991–1993), expanded uncertainties of spectral irradiance at 310 nm are between 6.4% and 9.2% and are dominated by uncertainties related to irradiance calibration, stability, wavelength errors, and unexplained diurnal variations at short wavelengths, which contribute to the uncertainty mostly at large SZAs. For volumes 5A–14 (1994–2005), expanded uncertainties of spectral irradiance at 310 nm are between 6.4% and 6.8%.

[24] At longer wavelengths, the overall uncertainty is governed by the uncertainty of the cosine error correction. This is a problem particularly during periods of varying cloudiness, when it is difficult to determine whether the cosine correction factor for clear or overcast sky should be applied. Expanded uncertainties for spectral irradiance at 600 nm range between 4.8% for overcast conditions and 11.4% for periods with variable cloudiness and large SZA. Expanded uncertainties for erythemal irradiance (i.e., spectral irradiance weighted with the CIE action spectrum for sunburn [*McKinlay and Diffey*, 1987]) and DNA-damaging irradiance (action spectrum by *Setlow* [1974]) vary between 5.8% and 6.6% (5.8–9.2% for volumes 2–4), and are only slightly influenced by sky condition.

[25] Data of several periods have larger uncertainties than indicated above. A summary of these periods can also be found at the version 2 Web site.

## 2.6. Self-Consistency of Version 2 Data

[26] Clear-sky measurements of different years were compared to check the self-consistency of version 2 data. In the first step of the analysis, ratios of measured and modeled spectra were calculated from all data associated with clear-sky periods when the Sun was more than 10° above the horizon. The resulting ratio spectra are denoted  $q_{V2}(\lambda)$ . The comparison with the model is helpful to remove the dependence of known parameters such as SZA, total ozone, and albedo from the measurement, which are different every year. It also alleviates the difficulty that clear skies occur in different periods for every year. Note that model results were part of the correction procedures used to generate version 2 data. For example, total ozone and albedo were retrieved from measured spectra and used as model input parameters. Version 2 data are therefore not independent from model results. Despite this interdependence, a comparison of measurement and model proved to be valuable in detecting problems of the measurements. Ratio spectra for every year can be found on the version 2 Web site.

[27] In the second step of the analysis, the median of ratio spectra  $q_{V2}(\lambda)$  was calculated on a wavelength-by-wavelength basis from all ratio spectra of a given year, and the procedure was repeated for all years. The resulting “median-ratio-spectra” are denoted  $M(\lambda, y)$  and vary between 0.95 and 1.02 for wavelengths larger than 320 nm with the exception of spectra of the years 1991–1993, which are affected by the large cosine error of the instrument for wavelengths larger than 490 nm.

[28] For the final step of the analysis, we consider the ratio  $Q(\lambda, y)$ , defined as:

$$Q(\lambda, y) = \frac{M(\lambda, y)}{\frac{1}{11} \sum_{y'=1995}^{2005} M(\lambda, y')} \quad (3)$$

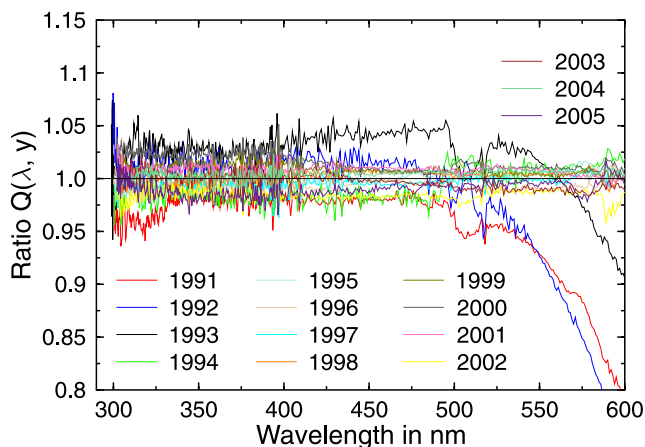


**Figure 2.** Q-ratios for the years 1991–2005 at Barrow.

The denominator of equation (3) is the average of all median-ratio-spectra from 1995 to 2005, which are not affected by the large cosine error of early data. Because of the construction of  $Q(\lambda, \gamma)$ , systematic differences between measurement and model, which affect all years equally such as those arising from the ETS used by the model, are ratioed out. These “Q-ratios” are shown in Figure 2 for every year. With the exception of data of the years 1991–1993, Q-ratios agree to within  $\pm 3\%$ , confirming that corrected measurements of the years 1994–2005 are on average consistent at the  $\pm 3\%$  level. Individual spectra from different years may have larger discrepancies as discussed above. The Q-ratio of the year 1994 shows a step of about 3.5% between 493 and 495 nm, which is partly an artifact of the insufficiently accurate correction of the monochromator’s Wood’s anomaly [Palmer, 2005] around 500 nm. Between 27 January 1994 and 9 June 1994 a different monochromator was used. Because of an insufficient number of clear-sky spectra, coefficients for the cosine and Wood’s anomaly correction could not be established with confidence for this short period.

### 2.7. Comparison of Version 0 and Version 2

[29] Version 2 data were compared with the original release “version 0.” A detailed comparison of the two versions is available on the version 2 Web site, focusing on nine spectral intervals in the UV and visible as well as erythemal [McKinlay and Diffey, 1987] and DNA-damaging [Setlow, 1974] irradiance. Differences are mostly caused by wavelength error and cosine error corrections. Differences between 300 and 310 nm are between  $-2\%$  and  $+22\%$  and are predominantly due to difference in the wavelength calibrations of the two versions. Disparities for data measured after 1997 are smaller than 5%. Above 310 nm, the difference of the two versions is due to the cosine error correction and the way spectra are assembled from the underlying raw data. Differences between version 0 and 2 peak at SZAs between  $70^\circ$  and  $80^\circ$ , depending on the spectral band. Erythemal and DNA-damaging dose rates from the version 2 data set are between 0 and 10% higher than version 0 data. Differences depend on SZA, year, and sky condition, among other causes. Differences for UV-A irradiance range between  $-5\%$  and  $+11\%$ . Differences for the integral of 400 to 600 nm are between  $-10\%$  and  $+20\%$

( $-5\%$  and  $+12\%$  for SZAs smaller than  $65^\circ$ ). Ratios of version 2 and version 0 data have different patterns for the periods 1991–1993 (volumes 2–4), spring of 1994 (volume 5A) and June of 1994 through 2005. Changes in the pattern are caused by exchange of the instrument’s cosine collectors in December 1993 and the installation of a different monochromator in the spring of 1994.

## 3. Climatology

### 3.1. Total Ozone

[30] Calculation of total ozone from UV spectra measured with the SUV-100 spectroradiometer at Barrow have already been presented by Bernhard *et al.* [2003]. Calculations were based on climatological profiles for Barrow and expanded ( $k = 2$ ) uncertainty in retrieved ozone values during clear skies ranged between 3.0% for summer and 5.2% for autumn. The largest contribution to the overall uncertainty stemmed from insufficient knowledge of the ozone profile, in particular at large SZAs. Bernhard *et al.* [2003] also compared SUV-100 ozone values from the period 1996–2001 with ozone measurements performed with a Dobson spectrophotometer by ESRL at their facility at Barrow. On average, SUV ozone values were higher than Dobson measurements by  $1.8 \pm 2.3\%$  ( $\pm 1\sigma$ ) in spring and  $0.9 \pm 1.8\%$  in autumn.

[31] Ozone values were recalculated as part of version 2 data processing. Version 2 ozone data are on average larger by  $0.6 \pm 0.4\%$  than the earlier calculation by Bernhard *et al.* [2003]. This difference is well within the uncertainty of the retrieval algorithm and caused by the slightly different set of model input parameters (e.g., surface albedo, AOD, Rayleigh-scattering optical depth) used for version 2. Figure 3 presents a comparison of version 2 SUV-100 and Dobson total ozone measurements for the period 1991–2004. SUV ozone values are higher than Dobson measurements by  $2.7 \pm 3.4\%$  on average. The ratio of the two data sets depends only very little on SZA and total ozone, indicating that the ozone profile climatology used in the inversion algorithm was adequate.

[32] There is a large annual cycle in total ozone (Figure 3c). Average total ozone is about 450 DU in early spring and gradually decreases to 300 DU in August and September. Several episodes of springtime ozone depletion have been observed in the past, most notably in 1997 and 2005 (Figures 3a and 3c). On 17 March 1997, total ozone was 315 DU, which is more than 100 DU below the typical ozone column for this time of the year. UV levels on this day remained small as solar elevations stayed below  $18^\circ$ . Similar low-ozone events occurring later in spring (e.g., 17 April 1997 and 29 April 2005) led to conspicuous spikes in UV (section 4.3).

### 3.2. Effective Surface Albedo

[33] Effective albedo is defined as the albedo of a uniform Lambertian surface, that, when used as input into a 1-D model, reproduces the measured spectrum [Lenoble *et al.*, 2004]. The albedo of fresh snow can be larger than 0.95 and is almost independent of wavelength between 290 and 600 nm [Grenfell *et al.*, 1994]. Photons reflected upward from the surface are partly scattered downward by Rayleigh-scattering on air molecules. Because of the wavelength dependence of

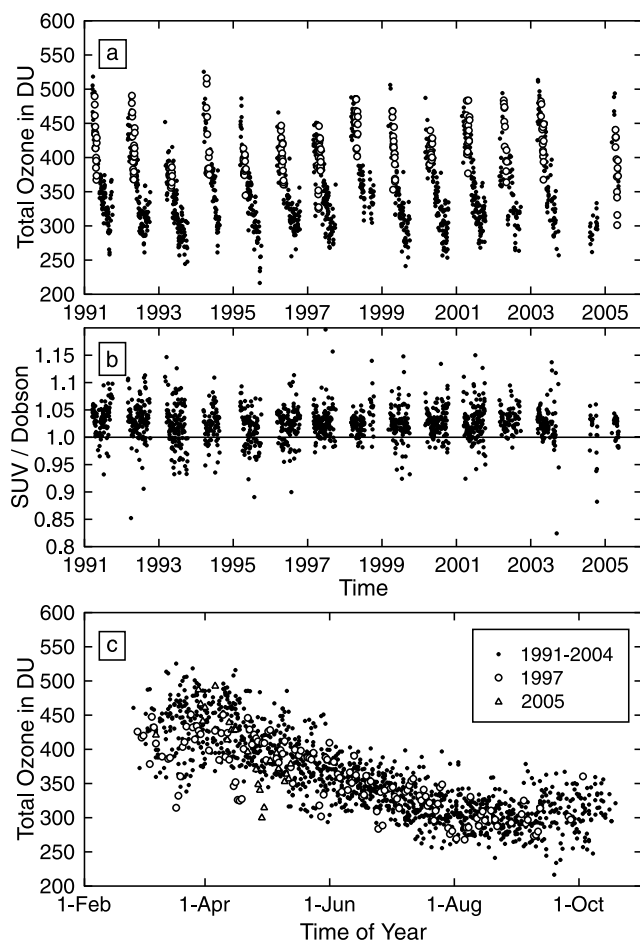


**Figure 3.** (a) Total ozone at Barrow calculated from SUV-100 UV spectra. Data from the period 10 April to 1 May of every year are indicated by open circles. (b) Ratio of SUV-100 and Dobson total ozone data as a function of time. (c) SUV-100 total ozone at Barrow as a function of time of year based on data of the years 1991–2005.

Rayleigh-scattering, albedo leads to a wavelength-dependent increase in surface UV with larger changes at shorter wavelengths. Utilizing this principle, effective albedo was calculated from clear-sky UV spectra with the method described by Bernhard *et al.* [2005b, 2006]. The  $1\sigma$ -uncertainty of retrieved albedo values is 0.1. This value is comparable to uncertainties of albedo calculations reported by Weihs *et al.* [2001].

[34] Under cloudy conditions, effective albedo cannot be calculated from our data with sufficient accuracy because albedo and cloud effects are closely coupled and have similar spectral signatures [Ricchiuzzi *et al.*, 1995]. For example, enhancement of UV-A irradiance in the presence of snow and clouds can either be interpreted as an increase in albedo or a decrease in cloud optical depth. In the absence of other data, effective albedo for cloudy days was linearly interpolated from the clear-sky data set. The albedo estimate is inevitably uncertain during long periods of persistent cloudiness. Clouds also modify the size of the area surrounding the measurement site that contributes to the albedo effect. For example, Degünther and Meerkötter

[2000] found that changes in surface albedo far away from the measurement site have a larger effect on irradiance when the sky is clear than when it is overcast. Estimating effective albedo for cloudy days from clear sky data is therefore subject to additional uncertainties when surface albedo is inhomogeneous. These are important caveats when interpreting the influence of albedo on UV irradiance under cloudy skies.

[35] Figure 4 shows effective surface albedo calculated from all available clear-sky spectra measured at Barrow between March 1991 and May 2005 for SZAs smaller than  $80^\circ$ . In March and April, albedo values are typically between 0.75 and 1.0. The average albedo is  $0.83 \pm 0.08$  ( $\pm 1\sigma$ ), but values below 0.6 were measured in spring of 2001 and 2002. Part of the variation is due to the uncertainty of the retrieval, but some variation is likely real and caused by aging of snow or changes in sea ice.

[36] Between May and June, snow starts to melt, leading to a gradual drop in albedo. Effective albedo is also affected by the extent of sea ice on the adjacent Chukchi Sea. Albedo is below 0.15 during August and September. Frequent cloud cover during these months limits the availability of clear-sky albedo data.

[37] The period of snowmelt exhibits a large year-to-year variability [Stone *et al.*, 2002]. For example, the date when effective albedo dropped below 0.45 for the first time in a given year (dashed line in Figure 4) varied between 23 May (year 2002) and 23 June [1992]. On 6 June, albedo was as high as 0.8 [2000] and as low as 0.2 [2003]. A change in albedo from 0 to 1 changes erythemal irradiance by up to 60% [ACIA, 2005]. The date of snowmelt is therefore expected to have a large effect on UV radiation at Barrow during months of May through July, when absolute UV irradiance at Barrow is at its highest.

### 3.3. Annual Cycles of UV and Visible Radiation

[38] After version 2 data for Barrow were generated and their quality confirmed, data were used to establish a climatology of ultraviolet and visible radiation. Figure 5 shows annual cycles for observations performed close to local solar noon (Figures 5a–5d) as well as daily doses (Figures 5f–5i) of four version 2 data products using data from the period February 1991 to May 2005. Short-wave

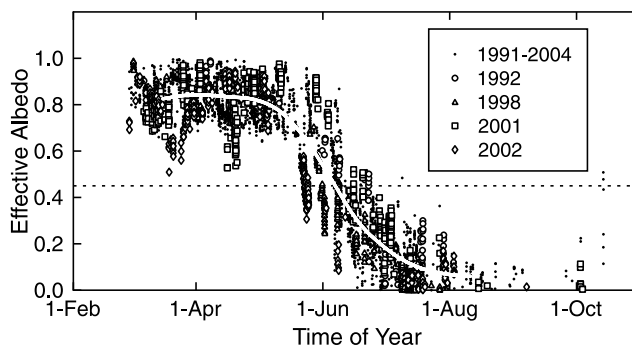


**Figure 4.** Effective surface albedo calculated from SUV-100 spectra sampled during clear skies at Barrow between 1991 and 2004. Data from the years 1992, 1998, 2001 and 2002 are emphasized. The white thin line is a smoothed fit to the data.

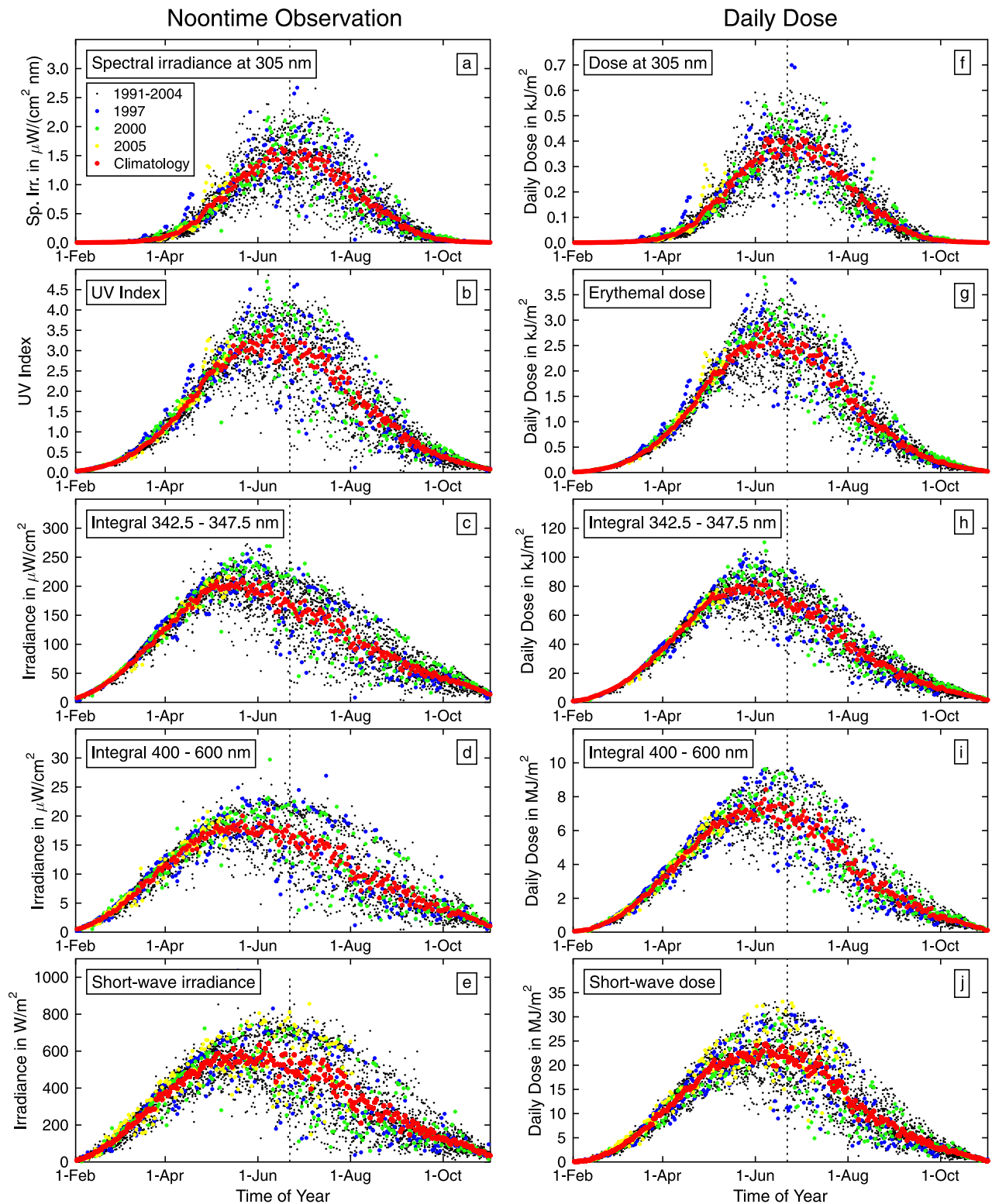


**Figure 5.** Annual cycles of (a–e) noontime observations and (f–j) daily doses of four version 2 data products as well as short-wave radiation measured at the ESRL station. Data are from the years 1991–2005, except for Figures 5d and 5i, which include data from the years 1994–2005 only. Measurements from the years 1997, 2000, and 2005, as well as climatological means are highlighted. Dashed vertical lines indicate solstice. Shown are spectral irradiance at 305 nm (Figure 5a), UV Index (Figure 5b), spectral irradiance integrated from 342.5 to 347.5 nm (Figure 5c), spectral irradiance integrated over 400 to 600 nm (Figure 5d), short-wave (0.285–2.8  $\mu\text{m}$ ) irradiance (Figure 5e), daily dose at 305 nm (Figure 5f), daily erythemal dose (Figure 5g), daily dose of integral 342.5–347.5 nm (Figure 5h), daily dose of integral 400–600 nm (Figure 5i), and daily short-wave dose (Figure 5j).

(integral of 0.285 to 2.8  $\mu\text{m}$ ) noontime irradiance and short-wave daily dose are also included in Figures 5e and 5j. These data sets were measured with Eppley Precision Spectral Pyranometers (PSP) at the ESRL station [CMDL, 2004; Dutton *et al.*, 2004].

[39] Noontime data from the SUV-100 spectroradiometer are based on spectral scans starting at 2200 UT, which are available for all years. Daily doses were calculated by integrating instantaneous measurements over 24 hour periods. Gaps in time series of two hours or less were filled via spline interpolation [Bernhard *et al.*, 2005a]. Days with gaps longer than two hours were excluded from further analysis. The four version 2 data products are spectral irradiance at 305 nm, erythral irradiance [McKinlay and Diffey, 1987] (represented by the UV Index [WMO, 1998; World Health Organization, 2002]), spectral irradiance integrated over 342.5 to 347.5 nm, and spectral irradiance integrated over 400 to 600 nm. Measurements on the same calendar day from different years were averaged to establish climatologies. These climatological mean values are also indicated in Figure 5.

[40] Figure 5 supports the following conclusions:

[41] 1. UV levels at 305 nm approximately peak at the solstice (Figures 5a and 5f). Highest measurements are from 24 and 26 June 1997 when total ozone was 285 DU, which is 50 DU below the climatological value for this period. Spikes in springtime UV at 305 nm, caused by abnormally low ozone, were observed in several years. Most notable events were detected on 20 May 1993, 31 May 1995, 18 April 1997, 27 May 1997, 22 May 2002, and 28 April 2005. The daily dose on 18 April 1997 was 0.18 kJ/m<sup>2</sup>, which is a factor of 2.6 larger than the climatological mean for this day and the largest relative enhancement of the data record. Doses of this magnitude are typically not observed before May.

[42] 2. Typical noontime UV Indices during summer vary between 2 and 4. The highest UV Index was 5.0 and observed on 7 June 2000 at 2218 UT. The highest erythral daily dose occurred on 6 June 2000. Total ozone on this day was 347 DU, which is close to the climatological mean for this day of 353 DU. Surface albedo was 0.8; the mean albedo for this day of the year is 0.45.

[43] 3. Radiation levels in the UV-A and visible exhibit a strong spring-autumn asymmetry (Figures 5c, 5d, 5h, and 5i). The climatological mean for the integral centered at 345 nm peaks on approximately 20 May, or 1 month before the solstice. The peak of the climatological mean of the 400–600 nm integral occurs about 1 June or 3 weeks before the solstice. A less pronounced spring-autumn asymmetry can also be seen in the annual cycle of the UV Index (Figure 5b) and erythral dose (Figure 5g).

[44] 4. Variability is considerably smaller during spring than during autumn.

[45] 5. Scatter in the visible is larger than scatter at 345 nm.

[46] 6. The seasonal pattern of short-wave pyranometer data (Figures 5e and 5j) is comparable to the pattern of the 400–600 nm integral (Figures 5d and 5i), but the variability is somewhat larger for the short-wave data sets.

[47] 7. Daily doses of the 400–600 nm and short-wave integrals have a well defined upper envelope, which is made up from measurements on clear-sky days (Figures 5i and 5j). Noontime irradiance of these integrals have a bimodal distribution with gaps between observations during clear and cloudy skies (Figures 5d and 5e). There are also

measurements above the clear-sky limit recorded during broken-cloud conditions.

[48] 8. Scatterplots of daily doses (Figures 5f–5j) exhibit less variability than noontime observations (Figures 5a–5e) and have a more pronounced summertime peak.

[49] 9. Climatological means of version 2 and short-wave data exhibit a discontinuity around 1 August. This may be caused by a general change in the weather regime occurring during this part of the year. We note that version 2 data products are independent of short-wave data, measured with ESRL pyranometers 2 km away from the spectroradiometer. Hence the discontinuity cannot be explained with data gaps or local effects.

[50] 10. Exceptionally thick clouds on 3 August 1997 led to very low noontime radiation levels.

### 3.4. Trends

[51] Long-term changes in UV, visible, and short-wave radiation were analyzed by calculating monthly averages of the noontime observations depicted in Figures 5a–5e. Only months with five or fewer missing days were used for the analysis. Version 2 data from June–September 1991, March 1993, and May–August 2004 were not used because of their increased uncertainty. Analysis of the 400–600 nm integral is restricted to the period 1994–2005 because of the large cosine error affecting data of earlier years. When comparing trends in the visible with trends at shorter wavelengths, the different lengths of the associated periods should be taken into account.

[52] Figure 6 shows the resulting time series of monthly average noontime observations. Trend lines were calculated for all data sets by linear regression and are also shown. Slopes of the trend lines (expressed in change per decade relative to the year 1990), their  $2\sigma$ -uncertainty, and regression coefficients  $R^2$  are given in the legend of Figure 6.

[53] Best estimates of trends vary between  $-23\%$  and  $+11\%$  per decade, depending on data product and month, are predominantly negative, but are generally not significant at the  $2\sigma$ -level. For April, May, and July, trend estimates are negative and range from  $-10$  to  $-17\%$  per decade for spectral irradiance at 305 nm. Best estimates for long-term changes in the UV-A and visible were slightly positive for these months. A negative trend at 305 nm that is not seen in the UV-A is indicative of a positive trend in total ozone. To confirm this suggestion, we estimated trends of total ozone from the SUV data set introduced in section 3.1. No statistically significant changes were found for any month of the 14-year period 1991–2004. The main reason is the large interannual variability in stratospheric ozone concentrations. Trend estimates for April, May, and July were  $3 \pm 6\%$ ,  $5 \pm 6\%$ , and  $3 \pm 8\%$ , respectively. These positive changes in total ozone are consistent with the observed negative trend estimates of UV-B irradiance.

[54] The year-to-year variability is similar for all data products plotted in Figure 6. This finding is in stark contrast with results of a similar analysis for McMurdo and South Pole where interannual variability was much larger in the UV-B than in the UV-A and visible because of the influence of the ozone hole [B04; Bernhard *et al.*, 2006]. Relative changes of short-wave irradiance from one year to the next are very similar to relative changes of the 400–600 nm integral. Since the two data sets were derived

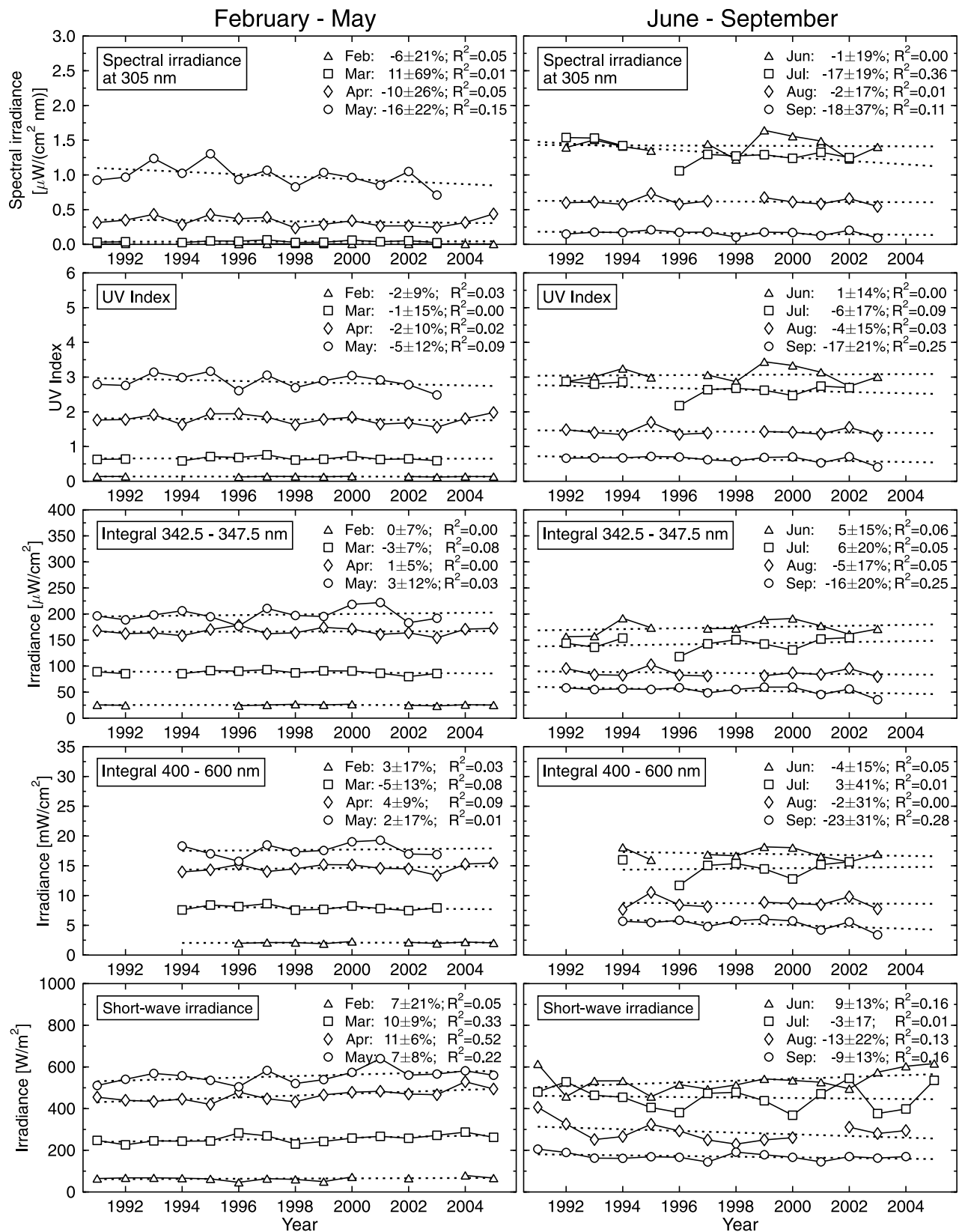


**Figure 6.** Time series of average monthly noontime irradiance for the months of (left) February–May and (right) June–September for five data products, indicated in the top left corner of each plot. Dashed lines are trend lines determined by linear regression. Best estimate of trend per decade,  $2\sigma$ -uncertainty of trend estimate, and regression coefficient  $R^2$  are also indicated.

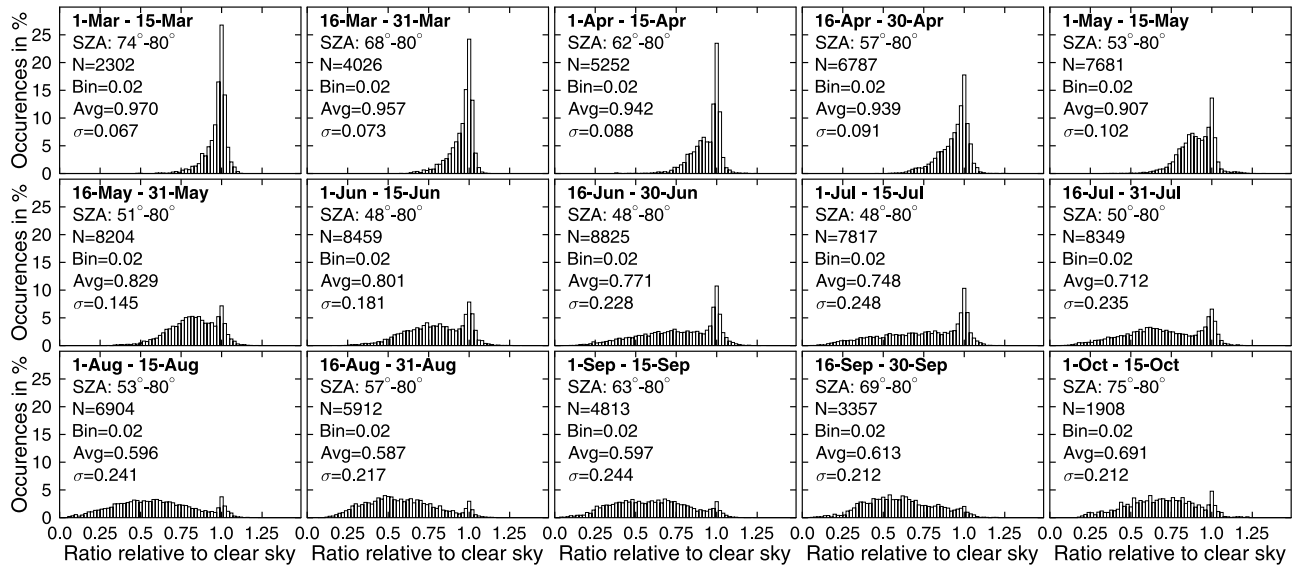


**Figure 7.** Frequency distributions of transmittance  $T(t)$  defined as the ratio of spectral irradiance integrated over 342.5–347.5 nm to the associated clear sky irradiance, calculated from measurements of the years 1995–2005. Each of the 15 plots refers to a different 2-week period as indicated in the top left corner of each plot. SZA-range, number of data points (N), width of the histogram columns (Bin), average (Avg), and standard deviation ( $\sigma$ ) of the distributions are also provided.

from independent instruments, the good agreement confirms that changes are real and not caused by possible sampling artifacts resulting from missing days.

[55] A similar trend analysis for daily doses instead of noontime irradiance is available at the version 2 Web site. As noted previously, daily doses calculated from days with gaps of two hours or more were not used. For some months, the trend analysis for daily doses therefore had to be based on a smaller number of years than the analysis for noontime observations. When the same number of years was available (i.e., April and June), trend estimates for noontime and daily integrated observations are almost identical. Trend estimates for months with a different number of available years can be quite different. For example, the trend in erythemal daily dose for May is  $-14\%$  per decade and significant at the  $2\sigma$ -level, whereas the trend estimate for the UV Index is only  $-5\%$  per decade and not significant. This is consistent with earlier studies showing that trend calculations are greatly affected by missing years, in particular when data from the start or end of the analysis period are absent [Weatherhead *et al.*, 1998]. This was the case for May.

### 3.5. Attenuation by Clouds

[56] Clouds are the dominant factor in reducing UV radiation. In a high-albedo environment, the influence of clouds is substantially altered by surface albedo [Ricchiuzzi *et al.*, 1995; Nichol *et al.*, 2003]. The modification of UV radiation by the combined effects of clouds and albedo are therefore discussed together and are quantified with transmittance  $T(t)$ , defined as

$$T(t) = \frac{E_{M,345}(t)}{E_{C,345}(t)} \bigg/ \sum_{\bar{t}_{\text{ev}}(t), p_i(t), \text{CS}} \frac{1}{n} \frac{E_{M,345}(\bar{t})}{E_{C,345}(\bar{t})}. \quad (4)$$

$E_{M,345}(t)$  is measured spectral irradiance integrated over 342.5–347.5 nm at time  $t$ , and  $E_{C,345}(t)$  is the associated clear-sky model irradiance. The denominator of equation (4) is the average ratio of measurement and model for clear sky conditions (CS) during year  $y$  and a 2-week period  $p_i$  (1–15 March, 16–31 March, ... 1–15 October). This term removes the observed bias between measurement and model for clear skies in any given year and period. Corrections vary between 0.90 and 1.00; the average correction is 0.96. Albedo used for the calculation of  $E_{C,345}(t)$  was determined from clear-sky spectra as described in section 3.2. In the next step,  $T(t)$ -values for the period 1–15 March and  $\text{SZA} < 80^\circ$  were selected from data of the years 1995–2005 and binned into 0.02-wide intervals to set up a frequency distribution. Similar distributions were constructed for each period  $p_i$  and are shown in Figure 7. Each plot in Figure 7 represents the climatology of transmittance relative to clear sky for a different part of the year.

[57] Distributions of many periods display a distinct maximum at  $T(t) = 1$ , marking clear-sky conditions. The clear-sky peak is most pronounced for the period 1–15 March and continually decreases as the year progresses. This indicates that clear-sky conditions and conditions with thin clouds are considerably more frequent in spring than in autumn. Distributions are much broader later in the year. For example, transmittances below 0.5 are virtually not observed between March and May. In contrast, distributions for August and September have a maximum at approximately  $T(t) = 0.5$  and transmittances below 0.1 were found. This can only be caused by optically thick clouds during periods when surface albedo is small.

[58] The average transmittance varies between 0.97 for the first 2 weeks of March and approximately 0.6 during August and September. The distributions' standard deviations increase from 0.07 in March to values larger than 0.21

for the months June–October. The uncertainty of these values is about 0.02 and is caused by uncertainties of the measurements and model input parameters. Enhancement of radiation beyond the clear sky value exceeds 10% in several months. These enhancements occur during situations when the disk of the Sun is not obstructed by clouds and additional radiation is reflected toward the instrument by clouds in the vicinity of the Sun [Mims and Frederick, 1994; Crawford *et al.*, 2003]. Enhancements seen at large SZAs (e.g., for the period 1–15 March) may partly be an artifact due to uncertainties of measurement, model, and cosine-error correction.

[59] A similar analysis for spectral irradiance integrated over 400–600 nm can be found on the version 2 Web site. These distributions are qualitatively similar to the distributions for the 342.5–347.5 nm integral, but confirm the observations from Figure 5 that the effect of clouds is larger in the visible than in the UV: average transmittances in the visible may be as low as 0.49 and distributions for August and September peak at 0.4 or below. Some rationale for the increased effect of clouds at longer wavelengths was presented by B04.

#### 4. Factors Affecting UV and Visible Irradiance

[60] UV and visible irradiance at the ground is affected by the SZA, clouds, Rayleigh scattering by O<sub>2</sub> and N<sub>2</sub>, the atmospheric ozone content (total column and profile), surface albedo, aerosols (type, optical depth, and profile), absorption by water vapor and trace gases such as NO<sub>2</sub> and SO<sub>2</sub>, and the distance between Sun and Earth [WMO, 2003]. The annual cycle caused by the variation in SZA is in good approximation symmetrical about the summer solstice (21 June). At Barrow, predominantly variations in total ozone, surface albedo, aerosols, and clouds modify the annual cycle and cause the asymmetry between spring and autumn that is apparent in Figure 5. The effect of these factors on noontime (2200 UT) irradiance at Barrow will be quantified in this section.

##### 4.1. Methodology

[61] Model calculations were used in sections 2 and 3 for quality control of version 2 data, for the retrieval of total ozone and albedo from measured spectra, and as reference for clear sky spectra. Here we go one step further and use the model to separate the different factors affecting UV. Specifically, we compare two data sets of model spectra. The first data set consists of clear-sky model spectra that complement version 2 measurements performed at 2200 UT. Model input parameters used for this data set represent the best estimate of the conditions at the time of the measurement (One exception is the effect of clouds, which is treated differently.) The second set of model spectra uses identical input parameters as the first set with the exception of the parameter whose effect on UV shall be analyzed. This parameter is set to a constant value. For example, to quantify the effect of total ozone on spectral irradiance at 305 nm, we ratioed version 2 model calculations of spectral irradiance at 305 nm with the result of similar calculations where the ozone column in the model was set to a constant value of 343 DU. This value is the median total column ozone for 21 June derived from observations of the years

1991–2005. Figure 8a shows the ratio of the two data sets as a function of time of the year. Using data from all available years, ratios for the same Julian day were averaged to set up a climatology of the effect of total ozone on spectral irradiance at 305 nm. This climatology is also indicated in Figure 8a. The effect of ozone on UV shows a pronounced annual cycle, which is anticorrelated with the annual cycle in total ozone (Figure 3c). For example, spectral irradiance in March is reduced on average by about a factor of two compared to the value that would be expected if the total ozone column in March were equal to that at the solstice. Similar calculations for the UV Index, spectral irradiance integrated over 342.5 to 347.5 nm, and spectral irradiance integrated over 400 to 600 nm are shown in Figures 8g, 9a, and 9g, respectively. We note that our method is similar to that used by Arola *et al.* [2003].

[62] To quantify the effect of surface albedo, we compared version 2 model results with similar calculations where surface albedo was set to zero. The resulting cycles are shown in Figures 8b, 8h, 9b, and 9h for the four data products analyzed. A climatology of the albedo effect was established following the procedure of the ozone effect by averaging ratios from the same Julian day of different years.

[63] The effect of aerosols on UV was analyzed in a similar way by comparing version 2 model data with model calculations where AOD was set to zero. Results are presented in Figures 8c, 8i, 9c, and 9i.

[64] The effect of clouds was quantified by comparing measured and modeled noontime irradiance. Model data were adjusted for the small bias between measurement and model observed during clear skies on the basis of the procedure described in section 3.5. As explained above, the effect of clouds is greatly modified by surface albedo. The analysis presented here quantifies the effect of clouds in the presence of snow covered ground. Ratios of measurement and model are shown in Figures 8d, 8j, 9d, and 9j for the four data products investigated.

[65] Monthly averages of the effects of ozone, albedo, aerosols, and clouds are presented in Table 2.

[66] The effect of the distance between Sun and Earth on irradiance was also modeled. The irradiance outside the Earth's atmosphere is smallest on 4 July when the Sun is farthest away from Earth (aphelion). The effect of the Sun-Earth distance is therefore not completely symmetrical about the solstice. Ground based irradiance is enhanced by approximately 4.5% in March and 4.0% in October compared to the value on the solstice.

[67] The climatological cycles of the effects of ozone, albedo, aerosols, clouds, and Sun-Earth distance on UV were then normalized to one at the solstice and plotted on the same scale (Figures 8e, 8k, 9e, and 9k). By multiplying the values of all cycles, the combined effect of the factors affecting UV and visible irradiance was estimated and is indicated by red lines in Figures 8e, 8k, 9e, and 9k. For example, spectral irradiance at 305 nm in March is reduced by approximately 25% compared to the value that would be expected if the values of all factors affecting UV were equal in March and at the solstice. The figures also allow assessment of the difference in irradiance between spring and autumn and identification of the factor responsible for the difference.

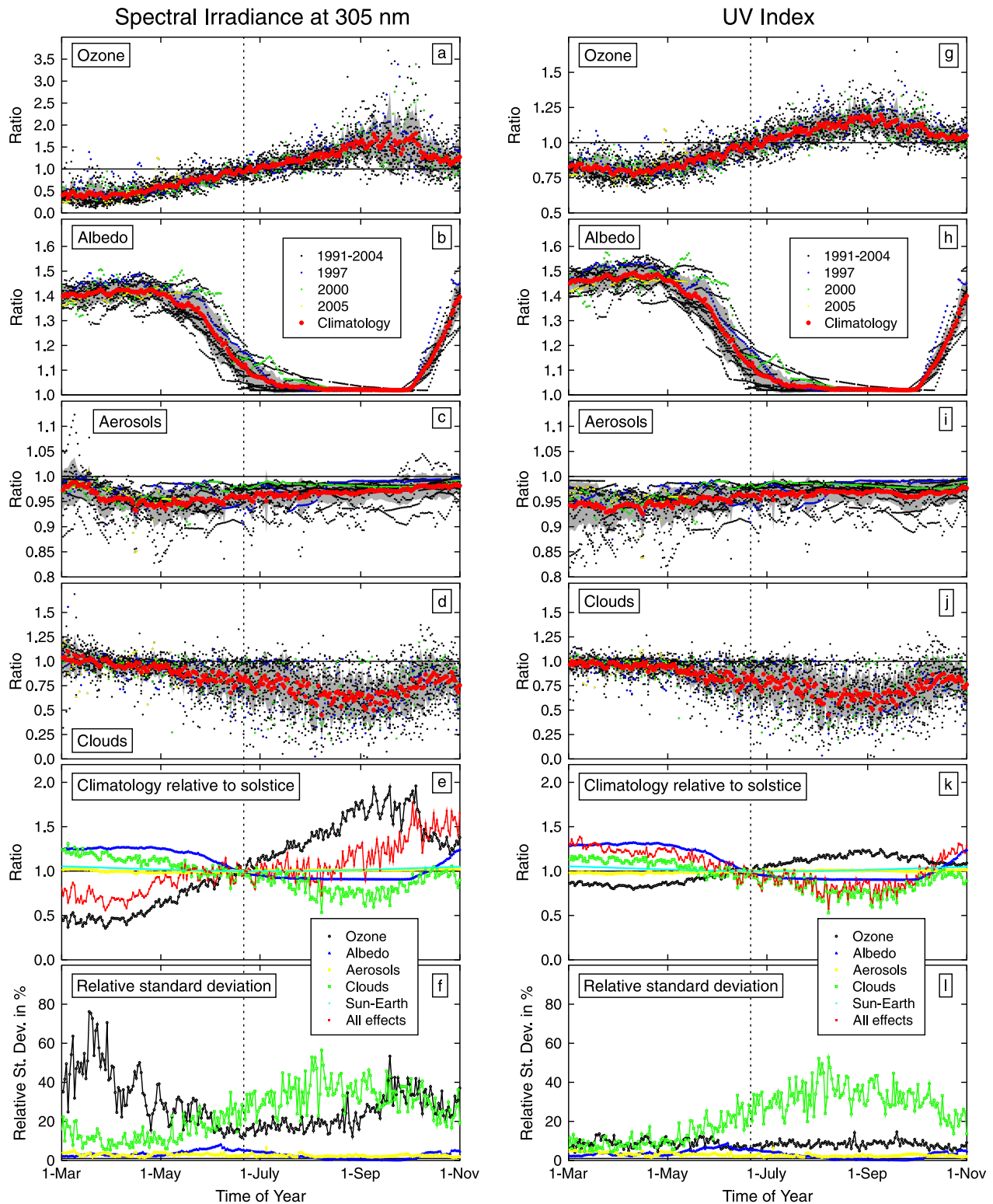


**Figure 8.** Effect of total ozone, surface albedo, aerosols, clouds, and Sun-Earth distance on (a–f) spectral irradiance at 305 nm and (g–l) the UV Index. All noontime spectra of the years 1991–2005 were evaluated. Data of the years 1997, 2000, and 2005, as well as climatological means are highlighted. Gray shading in Figures 8a–8d and 8g–8j indicates the range of mean  $\pm 1\sigma$ . Vertical dashed lines indicate the solstice (21 June). Shown are the ratio of version 2 clear-sky model data to similar model data but with total ozone set to 343 DU (Figures 8a and 8g), surface albedo set to 0 (Figures 8b and 8h), and aerosol optical depth set to 0 (Figures 8c and 8i). Figures 8d and 8j show the ratio of measured and modeled version 2 data. Figures 8e and 8k show climatological mean data normalized to 1 at solstice. Figures 8f and 8l show the relative standard deviation (i.e., ratio  $\sigma/\text{mean}$ ).

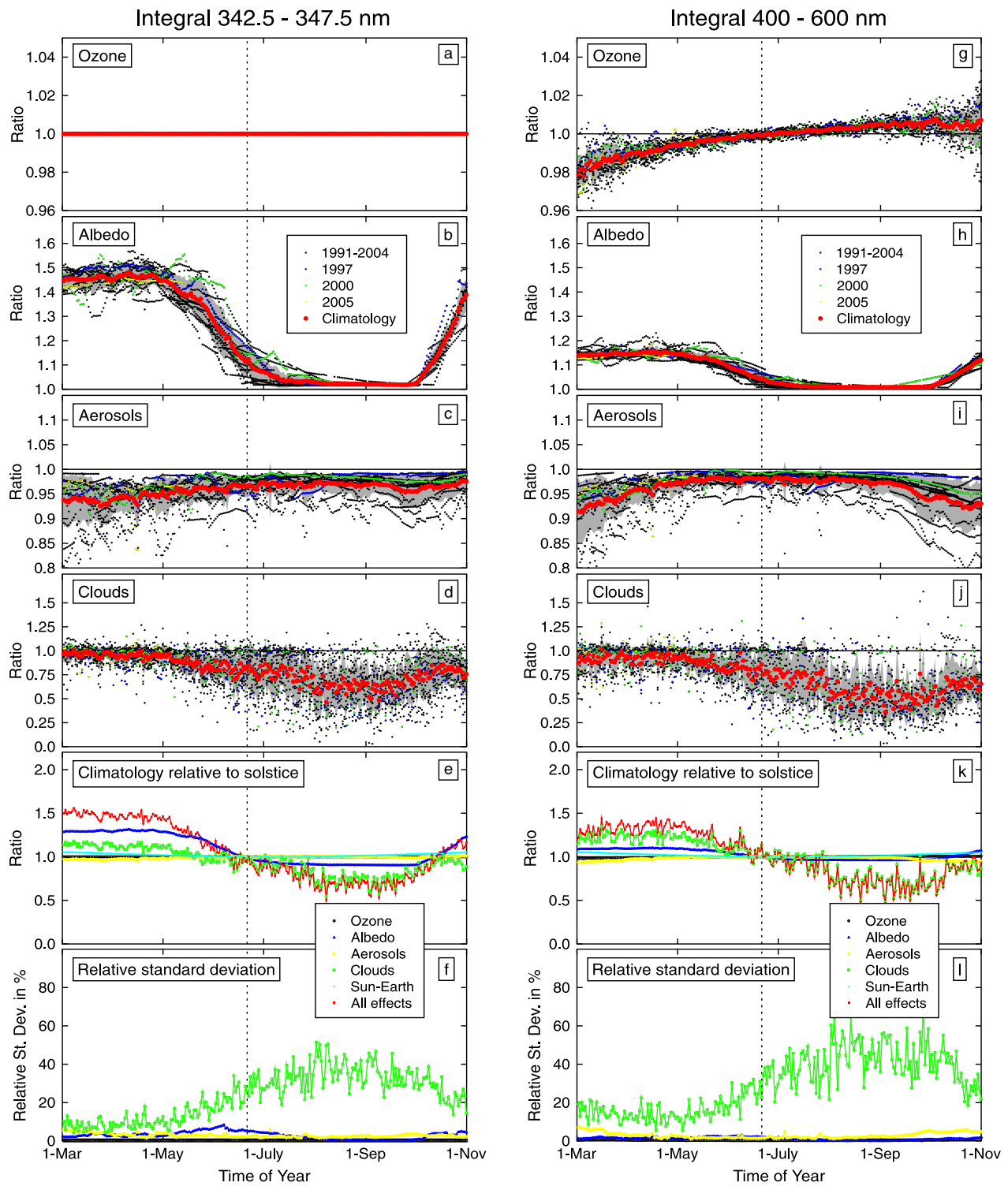


**Figure 9.** Same as Figure 8 but for spectral irradiance integrated (a–f) between 342.5 and 347.5 nm and (g–l) between 400 and 600 nm. Data of Figure 9j are based on the years 1994–2005 only.

[68] The year-to-year variability of the factors affecting UV was estimated in the final step of the analysis. The standard deviation of all ratios for a given Julian Day was calculated and divided by the climatological value of this day. The resulting relative standard deviations are plotted in Figures 8f, 8l, 9f, and 9l. Monthly averages are provided in

Table 2. We note that these values are independent from the normalization chosen. For example, the values for the relative standard deviation of the ozone effect would not change if we had selected a value other than 343 DU as the reference ozone column.

**Table 2.** Monthly Climatology of Effect of Ozone, Albedo, Aerosol, and Clouds on UV and Visible Noontime Irradiance at Barrow

Month	$E_{305}$				$E_{UVI}$				$E_{345}$				$E_{VIS}$			
	Ozone	Albedo	Aerosol	Cloud												
<i>Monthly Average of Effect, Referenced to Total Ozone = 343 DU, Surface Albedo = 0, No Aerosols, Clear Sky</i>																
Mar	0.409	1.408	0.972	1.010	0.817	1.466	0.940	0.973	1.000	1.455	0.936	0.968	0.985	1.144	0.933	0.926
Apr	0.479	1.419	0.949	0.945	0.802	1.479	0.942	0.948	1.000	1.464	0.945	0.947	0.991	1.149	0.963	0.926
May	0.707	1.354	0.949	0.871	0.870	1.393	0.952	0.875	1.000	1.380	0.957	0.873	0.996	1.125	0.979	0.873
Jun	0.927	1.149	0.957	0.801	0.965	1.159	0.960	0.805	1.000	1.152	0.965	0.804	0.999	1.054	0.980	0.795
Jul	1.141	1.041	0.963	0.750	1.062	1.042	0.965	0.755	1.000	1.040	0.968	0.752	1.001	1.015	0.978	0.710
Aug	1.413	1.023	0.968	0.628	1.142	1.024	0.969	0.632	1.000	1.022	0.970	0.628	1.003	1.008	0.976	0.546
Sep	1.594	1.020	0.972	0.637	1.133	1.021	0.966	0.646	1.000	1.020	0.963	0.633	1.005	1.009	0.960	0.511
Oct	1.323	1.191	0.980	0.796	1.058	1.195	0.969	0.795	1.000	1.188	0.966	0.781	1.005	1.063	0.933	0.627
<i>Variability Expressed as Monthly Averaged Relative Standard Deviation</i>																
Mar	52%	3%	3%	12%	9%	3%	4%	8%	0%	3%	5%	8%	1%	2%	5%	15%
Apr	34%	3%	3%	10%	9%	3%	3%	9%	0%	3%	3%	10%	0%	2%	3%	13%
May	25%	5%	3%	15%	9%	5%	3%	14%	0%	5%	3%	14%	0%	2%	2%	15%
Jun	15%	6%	3%	25%	7%	6%	3%	24%	0%	6%	2%	25%	0%	2%	2%	27%
Jul	17%	3%	3%	33%	8%	3%	3%	32%	0%	3%	2%	32%	0%	1%	2%	37%
Aug	20%	1%	2%	38%	8%	1%	2%	37%	0%	1%	2%	38%	0%	0%	2%	47%
Sep	32%	0%	2%	35%	9%	0%	2%	34%	0%	0%	3%	35%	0%	0%	3%	46%
Oct	30%	4%	2%	28%	7%	4%	2%	25%	0%	3%	3%	26%	1%	1%	5%	35%

## 4.2. Interpretation

[69] The information contained in Figures 8 and 9 will be discussed in more detail below. We use the symbols  $E_{305}$ ,  $E_{UVI}$ ,  $E_{345}$ , and  $E_{VIS}$  to refer to the data products spectral irradiance at 305 nm, the UV Index, and spectral irradiance integrals of 342.5–347.5 nm and 400–600 nm, respectively.

[70] The effect of total ozone is largest for  $E_{305}$ .  $E_{345}$  is not affected because ozone virtually does not absorb radiation between 342.5 and 347.5 nm. Ozone absorption in the Chappuis band [Bass and Paur, 1985] has a small effect on  $E_{VIS}$  (Figure 9g).

[71] High surface albedo caused by snow cover can enhance UV irradiance by up to 57% (Figures 8b, 8h, and 9b). The effect of albedo is similar for  $E_{305}$ ,  $E_{UVI}$ ,  $E_{345}$ , but substantially smaller for  $E_{VIS}$  because of the wavelength dependence of Rayleigh scattering (section 3.2). The albedo effect is slightly smaller for  $E_{305}$  than for  $E_{UVI}$  since radiation at 305 nm that is reflected upward by the surface and backscattered by the atmosphere is more efficiently absorbed by tropospheric ozone than  $E_{UVI}$ .

[72] Aerosols lead to reductions of  $E_{UVI}$ ,  $E_{345}$ , and  $E_{VIS}$  of typically 5% with maximum reductions of up to 20% (Figures 8i, 9c, and 9i). The aerosol effect is more pronounced in spring than in autumn because of Arctic haze events, which are more frequent during the first half of the year [Bodhaine and Dutton, 1993].

[73] The effects of albedo and aerosols sometimes increase linearly for several days in Figures 8 and 9. This artifact is due to the availability of albedo and AOD measurements during clear-sky periods only, and the fact that data for cloudy periods were calculated by linear interpolation.

[74] Enhancement of surface UV may occur at short wavelengths and large SZAs when scattering by stratospheric aerosols located within or above the stratospheric ozone layer reduces the photon path through the ozone layer [Davies, 1993]. This was observed in March and October of the years 1991–1994 when stratospheric aerosols from the Mt. Pinatubo eruption sometimes led to an increase of  $E_{305}$ . The magnitude of the enhancement largely depends on the

relative altitudes of the scatterer (aerosol) and the absorber (ozone). The enhancement indicated in Figure 8c is subject to uncertainty since the vertical profile of Pinatubo aerosols was not measured at Barrow.

[75] The effect of clouds is similar for all data products, albeit slightly larger for  $E_{VIS}$ ; consistent with the analysis presented in section 3.5.

[76] We now compare the relative importance of the annual cycles of ozone, albedo, aerosol and cloud effects for the four data products. The annual ozone cycle is the dominant factor in modifying  $E_{305}$  (Figure 8e). The combined effects of albedo and clouds compensate the ozone cycle between May and August. The red curve in Figure 8e, which represents the combined effects of all cycles, is virtually flat for this period. This explains the good symmetry of  $E_{305}$  about the solstice noted previously. For  $E_{UVI}$ , the cycles for albedo and cloud effects outweigh that for ozone, enhancing  $E_{UVI}$  in spring and reducing it in the autumn (Figure 8k). This is the reason for the slight asymmetry of the UV Index climatology that was shown in Figure 5b.

[77] The cycles of albedo and cloud effects are the dominant factors in modifying  $E_{345}$  (Figure 9e). These cycles are also responsible for the pronounced seasonal asymmetry of measurements at 345 nm shown in Figure 5c. The spring-autumn asymmetry is smaller for  $E_{VIS}$  because of the smaller albedo effect. The seasonal variation due to changing albedo outweighs the effect of clouds for all three UV data products; for  $E_{VIS}$ , the effect of clouds is dominant. Changes in UV and visible radiation caused by variations in aerosols and the Sun-Earth distance are small compared to the effects of ozone, albedo and clouds. The effect of variation in surface pressure on UV was also analyzed and found to be smaller than  $\pm 1\%$  ( $\pm 1\sigma$ ). The vertical column of  $\text{NO}_2$  averaged over 70–80° northern latitudes varies between  $1 \times 10^{15}$  molecules/cm<sup>2</sup> (or 0.03 DU) in winter and  $6 \times 10^{15}$  molecules/cm<sup>2</sup> (0.22 DU) in summer [Richter et al., 2005]. Resulting changes in UV were calculated and are smaller than 0.5%. Absorption by water

vapor becomes significant at wavelengths above 580 nm only, and is not discussed here.

[78] The year-to-year variation is mostly caused by variations in total ozone and cloudiness. For  $E_{305}$ , the variability is largest during March and April, when episodes of low total ozone can lead to large relative enhancements of UV (Figure 8f). The variability in cloud cover is the dominating effect between July and mid-September. For  $E_{UV1}$ , year-to-year variability in March and April is comparatively small and caused in similar parts by ozone and cloud cover (Figure 8l). Change in cloud cover is the dominant factor between June and October. For  $E_{345}$  and  $E_{VIS}$ , variability in cloud cover is dominant for all months and can reach more than 50% in autumn (Figures 9f and 9l). Variability of the albedo effect is largest in June during the period of snowmelt, when the relative standard deviation can reach 8%.

## 5. Discussion

[79] In Figures 8e, 8k, 9e, and 9k, we multiplied the cycles of all factors modifying UV and visible irradiance to calculate their combined effect. We note that this is an approximation as not all effects are independent of each other. For example, the attenuation by clouds greatly depends on surface albedo; enhancement of  $E_{305}$  by stratospheric aerosols depends on the ozone column below the aerosol layer; and the change of UV radiation as a function of total ozone also depends on SZA [Micheletti *et al.*, 2003].

[80] The enhancement of the clear-sky UV Index by surface albedo decreases on average from 40% on 18 May to 13% on 18 June in response to snowmelt. The melt date in northern Alaska is now 8 days earlier than it was during the mid-1960s because of decreased snowfall in winter, warmer spring conditions, and changes in regional circulation patterns [Stone *et al.*, 2002]. In order to estimate the effect of the changing melt date on the clear-sky UV Index, we shifted the albedo climatology shown in Figure 8h by 8 days and calculated the ratio of the unshifted and shifted curves. The change in snowmelt timing mainly affected the period 24 May to 19 July. The maximum reduction of the clear-sky UV Index is 7% and occurred between 2 and 17 June. The effect may be larger for all-sky conditions because of increased cloud attenuation when albedo is low. Changes in sea ice coverage that have occurred during the last 40 years have likely affected albedo and UV also. Quantification of this effect is beyond the scope of this paper. Global warming will likely advance the date of snowmelt further and lead to reduced sea ice cover, particularly during the summer [ACIA, 2005]. This will likely reduce summertime surface UV further.

[81] The presence of volcanic aerosols in the stratosphere following the eruption of Mt. Pinatubo increased  $E_{305}$  between autumn of 1991 and 1994 (Figure 8c). The magnitude of the enhancement largely depends on the aerosol profile [Davies, 1993]. Measurements of the aerosol profile at Barrow are not available. To quantify the effect of the profile on  $E_{305}$ , we compared several spectra measured in spring of 1992 and 1993 with model calculation using different aerosol profiles. Model results for wavelengths shorter than 305 nm clearly exceeded the measurements when the peak concentration of the aerosol layer was placed at 20 km. When the peak altitude was reduced to 17 km, we

found good agreement between measurement and model. This result is consistent with measurements of the aerosol profile at Kiruna, Sweden (68°N, 20°E) by *Deshler and Oltmans* [1998] who report that the top of the volcanic aerosol layer in 1993 and 1995 was near 500 K potential temperature (approximately 20 km altitude). Version 2 model calculations of  $E_{305}$  generally compare well with measurements during most of the period affected by the Pinatubo aerosol, indicating that the parameterization of the aerosol profile was appropriate. One exception is March 1992, when measurements of  $E_{305}$  exceeded the model by 5–10%. The enhancement by aerosols was likely underestimated by the model during this period. We point out that the enhancement only occurs at large SZAs when absolute UV levels are small and therefore has little practical consequence.

[82] Trend estimates for UV and visible radiation varied between –23% and +11% per decade, depending on data product and month, are predominantly negative, but are generally not significant at the  $2\sigma$ -level. This has several reasons: first, no significant trends in total ozone were observed for the period 1991–2004; second, large interannual variability of total ozone and cloudiness (Figure 8) masks long-term changes in UV; third, measurement uncertainties (section 2.5.) and data gaps further reduce the significance of trends; and last, a period of 14 years must still be considered short for the detection of trends in UV. For example, *Weatherhead et al.* [1998] have shown that 15 to more than 20 years of data are typically required to detect trends in erythral UV irradiance of 5% per decade.

[83] *Gurney* [1998] analyzed version 0 Barrow data from the years 1991–1995 and found large increases in noontime UV-B irradiance over most of the daylight year. At 305 nm, he found average annual increases ranging between 3 and 10% per year for all months except June. These increases were attributed to decreases in total ozone and probably related to the high stratospheric aerosol content following the eruption of Mt. Pinatubo in 1991 [WMO, 2003]. Our study indicates that UV irradiance returned to lower levels after the aerosol was removed from the stratosphere.

[84] *Díaz et al.* [2003] reconstructed daily doses of DNA-damaging and erythral irradiances for Barrow using satellite total ozone observations and pyranometer data of the years 1979–2000. The method was validated by comparing reconstructed data of the years 1993–1998 with version 0 NSF network data. Monthly means were calculated from daily doses and used to analyze changes in UV that may have occurred over time. Monthly mean daily doses of the years 1979–1986 varied within a range of  $\pm 30\%$  relative to the average of monthly means calculated from data of the years 1979–1981. Monthly mean daily doses for March and April measured after 1986 showed a large year-to-year variability with increases of up to 110% for DNA damaging radiation and 60% for erythral radiation relative to the reference period 1979–1981. The study by *Díaz et al.* [2003] confirms that spring time ozone depletion started to affect UV levels at Barrow in the mid-1980s, prior to measurements of the NSF UV network.

[85] *Lakkala et al.* [2003] evaluated long-term (1990–2001) changes of spectral UV irradiance between 300 and 325 nm at Sodankylä, Finland (67°22'N, 26°38'E). No statistically significant changes were observed for any

month for this 12-year period. Changes in UV were also calculated for several subperiods of the 12-year time series. Trend estimates for these shorter periods differed greatly from changes determined for the entire period. The largest positive change was found for the period 1990–1997. This result is similar to the situation at Barrow where changes for the period 1991–2005 were moderate, but large increases in UV were observed for the period 1991–1995 [Gurney, 1998].

[86] *Arola et al.* [2003] analyzed variability of  $E_{305}$  due to changes in total ozone, albedo and cloudiness at Sodankylä. Wintertime surface albedo at this Arctic site is smaller than at Barrow because of pine forests in the vicinity of the instrument. Variations of the monthly average of  $E_{305}$  caused by ozone are 35%, 21%, and 14% for the months of April, May, and August, respectively. Variations due to year-to-year differences in albedo are 3% in April and 7% in May, which is the month when snowmelt occurs. These numbers compare well with the variability at Barrow summarized in Table 2. Variation caused by cloudiness during summer months is larger at Barrow than at Sodankylä.

[87] *Kylling et al.* [2000] studied the effects of snow and clouds on erythemal radiation doses at Tromsø, Norway (69°39'N, 18°57'E). They found that snow may increase the monthly erythemal dose by more than 20% compared to snow-free ground with albedo of 0.1. Albedo at Tromsø remained below 0.6 because the area is influenced by the Gulf Stream, which prevents the adjacent ocean from freezing over. The terrain around Tromsø is also inhomogeneous, consisting of open fjords surrounded by forested mountains. The presence of clouds reduced the monthly erythemal dose by 20–40%. Similar reductions were observed at Barrow between June and October (Table 2).

## 6. Conclusions

[88] Version 2 data from the NSF/OPP SUV-100 spectroradiometer located at Barrow have been produced and feature smaller uncertainties and a larger number of data products than the original release “version 0.” New data products include (but are not limited to) total ozone column and effective albedo for clear skies. Erythemal and DNA-damaging dose rates of the version 2 data set are 0–10% higher than version 0 data. Version 2 clear-sky measurements of different years are typically consistent to within  $\pm 3\%$ . Expanded uncertainties of erythemal and DNA-damaging irradiance vary between 5.8% and 6.6% (5.8–9.2% for volumes 2–4). Uncertainties at longer wavelengths are dominated by uncertainties of the cosine-error correction and can exceed 10% at 600 nm. Uncertainties are particularly large under broken clouds when it is difficult to determine whether the cosine correction factor for clear or overcast sky should be applied. Measurements at wavelengths larger than 490 nm from the years 1991–1994 are affected by a large cosine error, which could not be corrected. Affected data from this period should not be used.

[89] Measurements were complemented with radiative transfer model calculations. These calculations were used for cosine and wavelength error corrections; quality control; the retrieval of total ozone and albedo from measured spectra; the separation of the different factors affecting

UV and visible radiation; and clear-sky reference spectra. Particular attention was given to the parameterization of aerosols. For example, wavelength-dependent aerosol extinction was derived from measurements of Sun photometers and a pyrheliometer, and the aerosol profile was modified during periods affected by aerosols from the Pinatubo eruption.

[90] Values of total ozone calculated from measured UV spectra are higher than measurements of a nearby Dobson spectrophotometer by  $2.7 \pm 3.4\%$  on average. A similar comparison of SUV-100 and Dobson measurements at McMurdo and South Pole resulted in biases of  $1.0 \pm 3.4\%$  [Bernhard et al., 2006] and  $1.6 \pm 2.4\%$  [Bernhard et al., 2005c], respectively. Although the bias for Barrow is somewhat larger, it is still within the combined uncertainty of SUV-100 and Dobson ozone data [Bernhard et al., 2003].

[91] Effective surface albedo at Barrow has a pronounced annual cycle with measured values ranging between 0.75 and 1.0 during March and April, and decreasing to values below 0.15 in August and September after the snow has melted.

[92] A climatology of UV and visible radiation at Barrow was established, focusing on annual cycles, trends, and the effect of clouds. UV levels at 305 nm peak approximately on the solstice. However, large departures from the climatological mean were observed in spring during several episodes of abnormally low total ozone. These events can be caused by photochemical ozone destruction, particularly during years when the polar vortex is strong and stratospheric temperatures low, or by occasional transport of ozone-poor air masses from lower latitudes [Bojkov and Balis, 2001]. Typical noontime UV Indices during summer vary between 2 and 4. The highest UV Index observed was 5.0 and was measured on a summer day when surface albedo was unusually high. Radiation levels in the UV-A and visible exhibit a strong spring-autumn asymmetry. UV-A irradiance peaks on approximately 20 May, about 1 month before the solstice. Clouds reduce UV radiation at 345 nm on average by 4% in March and by more than 40% in August. Reductions exceeding 90% were observed on rare occasions in autumn. Year-to-year variability of UV-A and visible radiation is also considerably smaller during spring than during autumn. Statistically significant trends in UV were not found, but trend estimates tend to be negative.

[93] The effect of total ozone, albedo, aerosols, and clouds on spectral irradiance at 305 nm ( $E_{305}$ ), the UV Index ( $E_{UVI}$ ), and the spectral integrals of 342.5–347.5 nm ( $E_{345}$ ) and 400–600 nm ( $E_{VIS}$ ) was quantified with model calculations. The annual ozone cycle was found to be the dominant parameter modifying  $E_{305}$ , but the combined effects of albedo and clouds compensate most of the ozone influence. High surface albedo caused by snow cover enhanced UV irradiance by up to 57%. Aerosols led to reductions of 5% typically, but larger reduction were observed during Arctic haze events. Stratospheric aerosols from the Pinatubo eruption enhanced  $E_{305}$  for large SZAs, but the magnitude of the effect is uncertain because of insufficient data on the aerosol profile. For  $E_{UVI}$  and  $E_{345}$ , the cycles of albedo and clouds are responsible for a pronounced seasonal asymmetry. The spring-autumn asymmetry is smaller for  $E_{VIS}$  because of the smaller albedo effect. Year-to-year variations are mostly caused by varia-

tions in total ozone and cloudiness. However, long-term changes in surface albedo can have a marked impact on UV levels from May through July. The effects of all factors influencing UV are in qualitative agreement with similar results obtained at Tromsø and Sodankylä, two sites in the Scandinavian Arctic. More UV data from the Arctic, particularly from the Russian sector, would be needed for extending the conclusions of this study to other northern high-latitude regions.

[94] **Acknowledgments.** Measurements at Barrow were supported by the National Science Foundation's Office of Polar Programs via subcontracts to Biospherical Instruments Inc. from Antarctic Support Associates (ASA) and Raytheon Polar Services Company (RPSC). Robert Stone was partly supported by NOAA's Arctic Research Program under its Study of Environmental Arctic Change (SEARCH) project. D. Stotts of the Ukeagvik Iñupiat Corporation (UIC) and J. Kelly and J. Sonderup of the Polar Ice Coring Office (PICO) aided in the original establishment of the system. We wish to express our gratitude to Daren Blythe, Dan Endres, Malcolm Gaylord, Glen McConville, Don Neff, and Teresa Winter from the Global Monitoring Division (GMD) of NOAA's Earth System Research Laboratory (ESRL), who operated the SUV-100 spectroradiometer. Further support was provided by Glenn W. Sheehan, Robert (Bob) Bulger, and Henry Gucco from the Barrow Arctic Science Consortium (BASC). Dobson data were provided by Sam Oltmans, Bob Evans, and Dorothy Quincey from GMD/ESRL. AERONET data were provided by Brent Holben and obtained from the Web site <http://aeronet.gsfc.nasa.gov>. NOAA11 SBUV/2 profiles were obtained from NOAA/NESDIS with support from the NOAA climate and global change program.

## References

- Anderson, G. P., S. A. Clough, F. X. Kneizys, J. H. Chetwynd, and E. O. Shettle (1986), AFGL atmospheric constituents profiles (0–120 km), *Tech. Rep. AFGL-TR-86-0110*, Air Force Geophys. Lab., Hanscom Air Force Base, Mass.
- Arctic Climate Impact Assessment (2005), *Arctic Climate Impact Assessment*, 1042 pp., Cambridge Univ. Press, New York. (Available at <http://www.acia.uaf.edu/pages/scientific.html>)
- Arola, A., K. Lakkala, A. Bais, J. Kaurola, C. Meleti, and P. Taalas (2003), Factors affecting short- and long-term changes of spectral UV irradiance at two European stations, *J. Geophys. Res.*, *108*(D17), 4549, doi:10.1029/2003JD003447.
- Bass, A., and R. J. Paur (1985), The ultraviolet cross sections of ozone: 1. The measurement, in *Atmospheric Ozone*, edited by C. Zerefos and A. Ghazi, pp. 606–616, Springer, New York.
- Bernhard, G., C. R. Booth, and R. D. McPeters (2003), Calculation of total column ozone from global UV spectra at high latitudes, *J. Geophys. Res.*, *108*(D17), 4532, doi:10.1029/2003JD003450.
- Bernhard, G., C. R. Booth, and J. C. Ehranjian (2004), Version 2 data of the National Science Foundation's Ultraviolet Radiation Monitoring Network: South Pole, *J. Geophys. Res.*, *109*, D21207, doi:10.1029/2004JD004937.
- Bernhard, G., C. R. Booth, J. C. Ehranjian, and V. V. Quang (2005a), *NSF Polar Programs UV Spectroradiometer Network 2001–2002 Operations Report*, vol. 11.0, 200 pp., Biospherical Instrum., San Diego, Calif. (Available at <http://www.biospherical.com/NSF>)
- Bernhard, G., C. R. Booth, and J. C. Ehranjian (2005b), UV climatology at Palmer Station, Antarctica, in *Ultraviolet Ground- and Space-Based Measurements, Models, and Effects V*, edited by G. Bernhard et al., *Proc. SPIE Int. Soc. Opt. Eng.*, *5886*, 7-1–7-12.
- Bernhard, G., R. D. Evans, G. J. Labow, and S. J. Oltmans (2005c), Bias in Dobson total ozone measurements at high latitudes due to approximations in calculations of ozone absorption coefficients and air mass, *J. Geophys. Res.*, *110*, D10305, doi:10.1029/2004JD005559.
- Bernhard, G., C. R. Booth, J. C. Ehranjian, and S. E. Nichol (2006), UV climatology at McMurdo Station, Antarctica, based on version 2 data of the National Science Foundation's Ultraviolet Radiation Monitoring Network, *J. Geophys. Res.*, *111*, D11201, doi:10.1029/2005JD005857.
- Bodhaine, B. A., and E. G. Dutton (1993), A long-term decrease in Arctic haze at Barrow, Alaska, *Geophys. Res. Lett.*, *20*, 947–950.
- Bodhaine, B. A., N. B. Wood, E. G. Dutton, and J. R. Slusser (1999), On Rayleigh optical depth calculations, *J. Atmos. Oceanic Technol.*, *16*, 1854–1861.
- Bojkov, R. D., and D. S. Balis (2001), Characteristics of episodes with extremely low ozone values in the northern middle latitudes 1957–2000, *Ann. Geophys.*, *19*, 797–807.
- Booth, C. R., T. B. Lucas, J. H. Morrow, C. S. Weiler, and P. A. Penhale (1994), The United States National Science Foundation's polar network for monitoring ultraviolet radiation, in *Ultraviolet Radiation in Antarctica: Measurement and Biological Effects*, *Antarct. Res. Ser.*, vol. 62, edited by C. S. Weiler and P. A. Penhale, pp. 17–37, AGU, Washington, D. C.
- Climate Monitoring and Diagnostics Laboratory (2004), *Summary Rep. 27 2002–2003*, edited by R. C. Schnell, A.-M. Bugge, and R. M. Rosson, U.S. Dep. of Commer., Boulder, Colo.
- Cockell, C. S., K. Scherer, G. Homeck, P. Rettberg, R. Facius, A. Gugg-Helminger, C. Driscoll, and P. Lee (2001), Exposure of Arctic field scientists to ultraviolet radiation evaluated using personal dosimeters, *Photochem. Photobiol.*, *74*(4), 570–578.
- Crawford, J., R. E. Shetter, B. Lefer, C. Cantrell, W. Junkermann, S. Madronich, and J. Calvert (2003), Cloud impacts on UV spectral actinic flux observed during the International Photolysis Frequency Measurement and Model Intercomparison (IPMMI), *J. Geophys. Res.*, *108*(D16), 8545, doi:10.1029/2002JD002731.
- Damoah, R., N. Spichtinger, C. Forster, P. James, I. Mattis, U. Wandinger, S. Beirle, T. Wagner, and A. Stohl (2004), Around the world in 17 days—Hemispheric-scale transport of forest fire smoke from Russia in May 2003, *Atmos. Chem. Phys.*, *4*, 1311–1321.
- Davies, R. (1993), Increased transmission of ultraviolet radiation to the surface due to stratospheric scattering, *J. Geophys. Res.*, *98*(D4), 7251–7253.
- Degünther, M., and R. Meerkötter (2000), Influence of inhomogeneous surface albedo on UV irradiance: Effect of a stratus cloud, *J. Geophys. Res.*, *105*(D18), 22,755–22,761.
- Deshler, T., and S. J. Oltmans (1998), Vertical profiles of volcanic aerosol and polar stratospheric clouds above Kiruna, Sweden: Winters 1993 and 1995, *J. Atmos. Chem.*, *30*, 11–23, doi:10.1023/A:1006023729315.
- Diaz, S., D. Nelson, G. Deferrari, and C. Camilión (2003), Estimated and measured DNA, plant-chromosome and erythral-weighted irradiances at Barrow and South Pole (1979–2000), *Agric. For. Meteorol.*, *120*(1–4), 69–82.
- Dutton, E. G., and J. R. Christy (1992), Solar radiative forcing at selected locations and evidence for global lower tropospheric cooling following the eruptions of El Chichon and Pinatubo, *Geophys. Res. Lett.*, *19*(23), 2313–2316.
- Dutton, E. G., A. Farhadi, R. S. Stone, C. N. Long, and D. W. Nelson (2004), Long-term variations in the occurrence and effective solar transmission of clouds as determined from surface-based total irradiance observations, *J. Geophys. Res.*, *109*, D03204, doi:10.1029/2003JD003568.
- Engelsen, O., M. Brustad, L. Aksnes, and E. Lund (2005), Daily duration of vitamin D synthesis in human skin with relation to latitude, total ozone, altitude, ground cover, aerosols and cloud thickness, *Photochem. Photobiol.*, *81*, 1287–1290.
- Grenfell, T. C., S. G. Warren, and P. C. Mullen (1994), Reflection of solar radiation by the Antarctic snow surface at ultraviolet, visible, and near-infrared wavelengths, *J. Geophys. Res.*, *99*(D9), 18,669–18,684.
- Gueymard, C. A. (2004), The Sun's total and spectral irradiance for solar energy applications and solar radiation models, *Sol. Energy*, *76*(4), 423–453.
- Gurney, K. R. (1998), Evidence for increasing ultraviolet irradiance at Point Barrow, Alaska, *Geophys. Res. Lett.*, *25*(6), 903–906.
- Holick, M. (1996), Vitamin D and bone health, *J. Nutr.*, *126*, 1159S–1164S.
- Knudsen, B. M., and S. B. Andersen (2001), Longitudinal variation in springtime ozone trends, *Nature*, *413*, 699–700.
- Kurucz, R. L., I. Furenliid, J. Brault, and L. Testerman (1984), *Solar Flux Atlas From 296 to 1300 nm*, *National Solar Observatory Atlas*, vol. 1, Harvard Univ. Press, Cambridge, Mass. (Available at <ftp://ftp.noao.edu/fts/fluxat/>)
- Kylling, A., A. Dahlback, and B. Mayer (2000), The effect of clouds and surface albedo on UV irradiances at a high latitude site, *Geophys. Res. Lett.*, *27*(9), 1411–1414.
- Lakkala, K., E. Kyrö, and T. Turunen (2003), Spectral UV measurements at Sodankylä during 1990–2001, *J. Geophys. Res.*, *108*(D19), 4621, doi:10.1029/2002JD003300.
- Lehmann, B. (2005), The vitamin D<sub>3</sub> pathway in human skin and its role for regulation of biological processes, *Photochem Photobiol.*, *81*(6), 1246–1251.
- Lenoble, J., A. Kylling, and I. Smolskaia (2004), Impact of snow cover and topography on ultraviolet irradiance at the alpine station of Briancçon, *J. Geophys. Res.*, *109*, D16209, doi:10.1029/2004JD004523.
- Marshall, S. F., C. S. Covert, and R. J. Charlson (1995), Relationship between asymmetry parameter and hemispheric backscatter ratio: Implications of the climate forcing by aerosols, *Appl. Opt.*, *34*(27), 6306–6311.
- Mayer, B., and A. Kylling (2005), Technical note: The libRadtran software package for radiative transfer calculations—Description and examples of use, *Atmos. Chem. Phys. Disc.*, *5*, 1319–1381.

- Maykut, G. A., and P. E. Church (1973), Radiation climate at Barrow, Alaska, 1962–66, *J. Appl. Meteorol.*, *12*, 620–628.
- McKinlay, A. F., and B. L. Diffey (Eds.) (1987), A reference action spectrum for ultraviolet induced erythema in human skin, *CIE J.*, *6* (1), 17–22.
- Micheletti, M. I., R. D. Piacentini, and S. Madronich (2003), Sensitivity of biologically active UV radiation to stratospheric ozone changes: Effects of action spectrum shape and wavelength range, *Photochem. Photobiol.*, *78*(5), 461–465.
- Mims, F. M., and J. E. Frederick (1994), Cumulus clouds and UVB, *Nature*, *371*, 291.
- Moon, S. J., A. A. Fryer, and R. C. Strange (2005), Ultraviolet radiation, vitamin D and risk of prostate cancer and other diseases, *Photochem. Photobiol.*, *81*(6), 1252–1260.
- Neuber, R., et al. (1994), Latitudinal distribution of stratospheric aerosols during the EASOE winter 1991/92, *Geophys. Res. Lett.*, *21*(13), 1283–1286.
- Newman, P. A., J. F. Gleason, R. D. McPeters, and R. S. Stolarski (1997), Anomalous low ozone over the Arctic, *Geophys. Res. Lett.*, *24*(22), 2689–2692.
- Nichol, S. E., G. Pfister, G. E. Bodeker, R. L. McKenzie, S. W. Wood, and G. Bernhard (2003), Moderation of cloud reduction of UV in the Antarctic due to high surface albedo, *J. Appl. Meteorol.*, *42*(8), 1174–1183.
- Palmer, C. (2005) *Diffraction Grating Handbook*, 5th ed., 204 pp., Thermo RGL, Richardson Grating Lab., Rochester, N. Y.
- Ricchiuzzi, P., C. Gautier, and D. Lubin (1995), Cloud scattering optical depth and local surface albedo in the Antarctic: Simultaneous retrieval using ground-based radiometry, *J. Geophys. Res.*, *100*(D10), 21,091–21,104.
- Richter, A., F. Wittrock, M. Weber, S. Beirle, S. Köhl, U. Platt, T. Wagner, W. Wilms-Grabe, and J.P. Burrows (2005), GOME observations of stratospheric trace gas distributions during the splitting vortex event in the Antarctic winter 2002 Part I: Measurements, *J. Atmos. Sci.*, *62*(3), 778–785.
- Rosen, J. M., N. T. Kjöme, R. L. McKenzie, and J. B. Liley (1994), Decay of Mount Pinatubo aerosol at midlatitudes in the northern and southern hemisphere, *J. Geophys. Res.*, *99*(D12), 25,733–25,739.
- Schiermeier, Q. (2005), Arctic trends scrutinized as chilly winter destroys ozone, *Nature*, *435*, 6, doi:10.1038/435006.
- Seckmeyer, G., A. Bais, G. Bernhard, M. Blumthaler, C. R. Booth, P. Disterhoft, P. Eriksen, R. L. McKenzie, M. Miyauchi, and C. Roy (2001), Instruments to measure solar ultraviolet radiation. Part 1: Spectral instruments, *Global Atmos. Watch Rep. 127, WMO TD 1066*, World Meteorol. Organ., Geneva, Switzerland.
- Self, S., J.-X. Zhao, R. E. Holasek, R. C. Torres, and A. J. King (1996), The atmospheric impact of the 1991 Mount Pinatubo eruption, in *Fire and Mud: Eruptions and Lahars of Mount Pinatubo*, edited by C. G. Newhall and R. S. Punongbayan, pp. 1089–1115, Univ. of Wash. Press, Seattle.
- Setlow, R. B. (1974), The wavelength in sunlight effective in producing skin cancer: A theoretical analysis, *Proc. Natl. Acad. Sci. U. S. A.*, *71*(9), 3363–3366.
- Shettle, E. P. (1989), Models of aerosols, clouds and precipitation for atmospheric propagation studies, paper presented at Conference on Atmospheric Propagation in the UV, Visible, IR and MM-Region and Related System Aspects, NATO Adv. Group for Aerosp. Res. and Dev., Copenhagen.
- Stokstad, E. (2003), Nutrition: The vitamin D deficit, *Science*, *302*, 1886–1888.
- Stone, R. S., J. R. Key, and E. G. Dutton (1993), Properties and decay of stratospheric aerosols in the Arctic following the 1991 eruptions of Mount Pinatubo, *Geophys. Res. Lett.*, *20*(21), 2359–2362.
- Stone, R. S., E. G. Dutton, J. M. Harris, and D. Longenecker (2002), Earlier spring snowmelt in northern Alaska as an indicator of climate change, *J. Geophys. Res.*, *107*(D10), 4089, doi:10.1029/2000JD000286.
- United Nations Environmental Program (2003), Environmental effects of ozone depletion and its interactions with climate change: 2002 assessment; executive summary, *Photochem. Photobiol. Sci.*, *2*, 1–4.
- Vogelmann, A. M., and T. P. Ackerman (1992), Enhancements in biologically effective ultraviolet radiation following volcanic eruptions, *Nature*, *359*, 47–49.
- Weatherhead, E. C., et al. (1998), Factors affecting the detection of trends: Statistical considerations and applications to environmental data, *J. Geophys. Res.*, *103*(D14), 17,149–17,161.
- Webb, A. R., L. Kline, and M. F. Holick (1988), Influence of season and latitude on the cutaneous synthesis of vitamin D<sub>3</sub>: Exposure to winter sunlight in Boston and Edmonton will not promote vitamin D<sub>3</sub> synthesis in human skin, *J. Clin. Endocrinol. Metab.*, *67*(2), 373–378.
- Weih, P., et al. (2001), Modeling the effect of an inhomogeneous surface albedo on incident UV radiation in mountainous terrain: Determination of an effective surface albedo, *Geophys. Res. Lett.*, *28*(16), 3111–3114.
- World Health Organization (2002), *Global Solar UV Index: A Practical Guide*, 28 pp., Geneva, Switzerland.
- World Meteorological Organization (1998), Report of the WMO-WHO meeting of experts on standardization of UV Indices and their dissemination to the public, *Global Atmos. Watch Rep. 127*, Geneva, Switzerland.
- World Meteorological Organization (2003), Scientific assessment of ozone depletion: 2002, *Global Ozone Res. Monit. Proj. Rep. 47*, 498 pp., Geneva, Switzerland.
- Yoon, H. W., C. E. Gibson, and P. Y. Barnes (2002), Realization of the National Institute of Standards and Technology detector-based spectral irradiance scale, *Appl. Opt.*, *41*(28), 5879–5890.

G. Bernhard, C. R. Booth, and J. C. Eghamjian, Biospherical Instruments Inc., San Diego, CA 92110-2621, USA. (bernhard@biospherical.com)

E. G. Dutton and R. Stone, Global Monitoring Division, Earth System Research Laboratory, NOAA, Boulder, CO 80305, USA.